Analysis of Iron Losses in Electrical Machines

Development of Single Sheet Tester and Deterioration Model due to Laser Cutting of Machine Core Steel Lamination

Master's thesis in Electric Power Engineering

EMMA JOHANSSON

DEPARTMENT OF ELECTRICAL ENGINEERING

CHALMERS UNIVERSITY OF TECHNOLOGY
Gothenburg, Sweden 2022
www.chalmers.se

Master's thesis 2022

Analysis of Iron Losses in Electrical Machines

Development of Single Sheet Tester and Deterioration Model due to Laser Cutting of Machine Core Steel Lamination

EMMA JOHANSSON

Department of Electrical Engineering
Division of Electrical Power Engineering
Chalmers University of Technology
Gothenburg, Sweden 2022

Analysis of Iron Losses in Electrical Machines
Development of Single Sheet Tester and Deterioration Model due to Laser Cutting of Machine Core Steel Lamination
EMMA JOHANSSON

Supervisor: Sima Soltanipour, Volvo Cars Corporation
Examiner: Torbjörn Thiringer, Electrical Power Engineering

Master's Thesis 2022
Department of Electrical Engineering
Division of Electrical Power Engineering
Chalmers University of Technology
SE-412 96 Gothenburg
Telephone +46 31 772 1000

Gothenburg, Sweden 2022

Analysis of Iron Losses in Electrical Machines
Measurements and Modelling of Electromagnetic Deterioration due to Laser Cutting of Machine Core Steel Laminations
EMMA JOHANSSON
Department of Electrical Engineering
Chalmers University of Technology

Abstract

To improve the efficiency of electrical machines there is a desire to model the changes of the magnetic properties in the machine cores due to applied stress during manufacturing. In this thesis the laser cutting of machine core steel laminations was investigated as a manufacturing process by building and using a single sheet tester setup for measurements. To emulate the deterioration of the steel sheets, one permeability model and one iron loss model was developed based on measurements made on steel laminations that had been cut into different geometries. The mathematical models were then used to implement the influence of laser cutting into an FEM-model of a V-shaped IPM machine in COMSOL Multiphysics. The permeability model and iron loss model had an average error of 10 % and 7 % respectively. The machine simulation yielded a 40.45 % increase in hysteresis losses and 37.36 % decrease in eddy current losses for full load operation. For 75 % load operation the results were similair with a 47.10 % increase in hysteresis losses and a 41.19 % decrease in eddy current losses. The result of the simulation was discussed extensively in conjunction with the errors of the models and insecurities of the measurements. In summary, the modelling technique of the deterioration of the magnetic properties showed potential for a more precise prediction of iron losses in electrical machines. Further development is needed for a precise and useful model customized to the manufacturing processes and material of the machine in question.

Keywords: Single sheet tester, laser cutting, iron losses, FEM, IPM, manufacturing processes, electrical machine.

Acknowledgements

This master thesis marks the end of my studies at Chalmers. I am forever grateful for the opportunities and connections I have been given during my work here. First and foremost I want to thank my supervisor Sima Soltanipour and manager Anders Thulin at Volvo Cars for the opportunity to work with this project and the guidance during the entire thesis work. Secondly I want to thank my examiner Torbjörn Thiringer at Chalmers and Mats Leksell at KTH for the never ending feedback on our results during the whole process.

Moreover, I want to thank my thesis partner Rishabh Raj at KTH for a smooth collaboration on the project. A special thank you to Viktor Lindström and everyone in the CaseLAB at Chalmers for realising our design of the Single Sheet Tester frame. Additionally I would like to extend my gratitude to everyone at the Electric Drive Hardware System Department at Volvo Cars and the entire Electric Power Engineering Division at Chalmers who has always met our questions with support and enthusiasm.

Next I would like to thank Elias Kambrin and Anton Ingemansson for their feedback on the report. Finally I would like to thank my sister for our weekly lunches in the EDIT building during the thesis project, they always provided a well needed break from the project work and has become a highlight during my time at Chalmers.

Emma Johansson, Gothenburg, June 2022

Abbreviations

EDM	Electrical Discharge Machining
EM	Electrical Machine
FEM	Finite Element Method
IEC	International Electrotechnical Commission
IPM	Interior Permanent Magnet
LCR-meter	Inductance-Capacitance-Resistance-meter
RSST	Rotational Single Sheet Tester
SST	Single Sheet Tester

Nomenclature

μ_0	Permeability of vacuum
μ_r	Relative permeability
ρ	Mass density
A	Area
B	Magnetic flux density
f	Electrical frequency
H	Magnetic field
i	Current
k_{ec}	Eddy current coefficient
k_{exc}	Excess loss coefficient
k_{hyst}	Hysteresis loss coefficient
k_{SE}	Steinmetz loss coefficient
l_{eff}	Effective length
N	Number of turns
N_{cuts}	Number of cuts in sample
p_{ec}	Eddy current losses
p_{Fe}	Iron loss density
p_{hyst}	Hysteresis losses
T	Time period
u	Voltage
V	Volume

Contents

1
Introduction

As the rate of the electrification of the vehicle industry is increasing so is the importance of designing efficient electrical machines. One impact that is usually overlooked at the simulation stage is the increased core losses due to the shaping and stacking techniques of the lamination sheets in the machine core. These additional losses can originate from different processes during the assembly of the machine core such as joining and cutting of the [1].

Extensive testing has been performed to determine the optimal cutting method of steel laminations. In [2] it is found that water-jet cutting and electrical discharge machining (EDM) has a lower impact on the magnetization and iron losses compared to mechanical and laser-cutting. This is contradicted in the findings of [3] where the conclusion is that water-jet cutting results in higher iron losses for an electrical machine compared to mechanical, laser and EDM cutting due to increased burr on the cutting edges. In [4] it is concluded that while the increase in losses for laser cutting is not insignificant, it is relatively small compared to the effects of guillotine cutting. It is also noted that punching has no serious effect on the iron losses. The explanation for the discrepancies in these results can be related to factors of the cutting equipment, the material of the laminations and the sheet geometry [5][6]. Additionally when investigating cutting techniques of laminations using single sheet testers (SST) and Epstein frames the cut samples are commonly joined together using glue. Thus this factor also needs to be taken into account when performing tests to determine the magnetic properties of steel laminations.

There is a desire to quantify the impact of these manufacturing processes for a more accurate simulation model in an early stage of the machine design process. In [7] a mathematical model was proposed to simulate the changing loss properties due to mechanical punching by dividing the cores of an electrical machine into layers with different material properties that represents different degrees of degradation. Mathematical models for permeability and iron losses are presented in [8] which utilizes high order elements to model the losses due to cutting of laminations. The developed loss model in this thesis was greatly influenced by these previously mentioned modelling methods.

1.1 Tasks

- Design and verification of SST setup

- Measurements of steel strips using SST
- Development of mathematical model for manufacturing defects
- Model implementation on an electrical machine(EM) simulated in COMSOL Multiphysics®.

1.2 Aim

The aim of this thesis was to investigate how a manufacturing method impact the steel sheets in the cores of electrical machines. Further, the aim was to model the loss impact of this process and implement the model in the cores of an EM using a finite element method (FEM)-based simulation software.

1.3 Scope

In this thesis the iron losses were modelled based on measurements made with a custom SST that subject the steel sheets to a unidirectional flux. From the design of the setup the SST is limited to only measure the unidirectional losses in the sample strips. Therefore, the loss models are based on the assumption that the flux in the electrical machines are unidirectional in each point i.e. rotational losses was not considered in this project. Further, the design of an electrical machine is out of scope for this thesis. Therefore, the FEM simulations were made on an existing reference machine. The simulation models were only implemented and analysed for discrete operating points of a interior permanent magnet (IPM) synchronous machine due to time limitations.

2

Ferromagnetic material properties

This chapter describes the origin of iron losses and frequently used loss models for ferromagnetic materials.

2.1 Iron losses

Iron losses occur due to the alternating flux in the ferromagnetic material, usually a core of a transformer or an electrical machine. Therefore also commonly denoted core losses. The following relation yields how the iron loss density can be calculated from instantaneous voltage and current [9]

$$p_{Fe} = \frac{1}{T\rho V}\int_0^T u(t)i(t)dt \tag{2.1}$$

where T is the time period, ρ is the mass density, V is the volume of the sample, u and i are the measured voltage and current. The two main contributions of iron losses are eddy current loss and hysteresis loss. Additional losses in the core are commonly referred to as excess losses.

2.1.1 Eddy current losses

From Faraday's law of induction it is known that a changing magnetic field will induce an electric field. If that electric field is occurring in a conductor, circulating currents are induced known as eddy currents. Due to the resistance in the material that the induced current experience, losses are generated through Joule heating [10]. To minimize these losses the cores of electrical machines are composed by insulated laminations that contains the induced currents and thereby minimize the losses.

2.1.2 Hysteresis losses

Hysteresis loss is related to the magnetization and demagnetization of the core. The current in the winding of a transformer or a machine is related to the magnetic field, or magnetic force, through Amperes law

$$H(t) = \frac{Ni(t)}{l_{\text{eff}}} \tag{2.2}$$

where H is the magnetic field, N is the number of turns of the excitation winding, and l_{eff} is the effective length of the sample. When the current in the circuit of a demagnetized material increase, the magnetic flux density increase until magnetic saturation occurs. During demagnetization the current decrease faster than the magnetic flux. When the inserted flux change direction some amount of flux is required to change the direction of the magnetization in the core [11]. Therefore the magnetic flux density still has a positive value when the field reaches zero, the material is still magnetized. For a full time period of sinusoidal flux density this yields a BH-loop where the width of the loop represents the hysteresis of the material.

2.2 Loss models

In order to estimate iron losses several loss models have been developed over time. One early model for iron losses presented by Steinmetz is found as

$$p_{Fe} = k_{SE} f^{\alpha} \hat{B}^{\beta} \tag{2.3}$$

where k_{SE}, α ,β are loss coefficients, $\hat{B}$ and f are peak magnetic flux density and frequency respectively. The model rely on the assumption that the magnetic flux density is a sinusoidal waveform [12]. Based on Steinmetz equation a number of other models have been developed, for instance Jordans separation model that separates the losses into hysteresis losses and eddy current losses

$$p_{Fe} = p_{hyst} + p_{ec} = k_{hyst} f \hat{B}^2 + k_{ec} f^2 \hat{B}^2 \tag{2.4}$$

where p_{hyst} represents hysteresis losses, p_{ec} is eddy current losses, k_{hyst} and k_{ec} are the respective loss coefficients.

However, the discovery that the calculated eddy current losses differed from the measured eddy current losses lead to the introduction of a third term for excess losses in Jordan's previous formula for iron losses. The following equation is called Bertottis loss model and is considered the most widely used approach for estimation of iron losses

$$p_{Fe} = p_{hyst} + p_{ec} + p_{exc} = k_{hyst} f \hat{B}^{\alpha} + k_{ec} f^2 \hat{B}^2 + k_{exc} f^{1.5} \hat{B}^{1.5} \tag{2.5}$$

where p_{exc} denotes the excess losses and k_{exc} the excess loss coefficient [13][14]. In (2.5) excess losses represents the additional losses caused by the domain wall motion due to the alternating magnetic field [9]. Jordans model in (2.4) also allowed for the development of one other separation model known as Pry and Beans loss model.

In electrical machines a significant amount of the iron losses around the stator slots is caused by the rotational flux densities in the core laminations [15]. In [16] Jacobs model was presented by rewriting (2.5) with a rotational loss factor to take the rotational losses into account. For full hysteresis curves the Preisach and Jiles-Atherton hysteresis models can be used for iron loss estimations [17]. These models are of a higher complexity compared to the Steinmetz model and its successors and generally have a higher accuracy which makes them suitable for more exact iron loss calculations [18].

3
Manufacturing processes

This chapter present some manufacturing processes that are used in the production of rotor and stator sheets of electrical machines and how they deteriorate the magnetic properties of electrical steel sheets. Two main processes during manufacturing of machines that are considered when discussing electromagnetic changes in the material are cutting and joining of laminations.

3.1 Cutting

There are several different factors that affects the observations when studying the deterioration of steel samples using different cutting techniques. Some of these factors are due to the settings of the tools for the cutting techniques, the grain size of the steel material, cutting geometry and the measurement method used to determine the degradation depth [5][6].

Punching and guillotine are two mechanical cutting methods that are relatively fast and does not apply any thermal stress to the steel. The material is punched out or cut by a guillotine into the desired shape. Punching is reportedly the general method used in large-scale production of electrical machines [19]. One mold is developed with the desired geometry and can be reused for a long time which reduce the manufacturing costs. Further, more than one lamination can be punched at once and the whole geometry is cut instantly. Laser-, water-jet cutting and EDM are common methods used to cut electrical steel sheets during development of prototypes since no custom machine punching tool is required [2]. EDM only allows for one sheet to be cut at a time compared to laser- and water cutting where multiple sheets can be stacked and cut simultaneously. The primary use of EDM is the cutting of samples used to investigate the magnetic properties of the steel due to the very small increase in loss. While all mechanical cutting techniques yield mechanical stress to the material, laser cutting has been shown to induce varying levels of thermal stresses depending of the properties of the laser cutter.

3.2 Pressing and joining

After cutting the laminations are stacked and pressed together. The mechanical stresses of pressing damages the insulation and deteriorates the the magnetic properties of the steel and results in higher eddy current and hysteresis losses [4]. The pressed laminations are then joined together to form the machine cores. Joining methods can be categorized into welding, mechanical and glue join [20]. While mechanical joining induce mechanical stress of the steel material as well as the insulation, welding causes a thermal stress to the laminations. Gluing has the advantage of not destroying the coating of the lamination and has overall been denoted the best method for joining laminations with regards to the magnetic properties [20].

4

Experimental setups

When conducting measurements regarding the magnetic properties of steel sheets there are several different approaches to be considered. For unidirectional losses a SST, or Epstein frame can be utilized but if circular or rotational losses are taken into consideration a toriod tester or rotational single sheet tester(RSST) can be used.

4.1 Single sheet tester

A standard SST consists of two identical U-shaped laminated iron cores, a primary excitation winding and a secondary winding. The windings are typically wound on the top and bottom core or on top of each other on a bobbin that surrounds the steel sample under test as displayed in Figure 4.1. To fulfill the standards of The International Electrotechnical Commission (IEC) for SSTs the latter alternative is required [21]. The secondary winding should in this case be wound underneath the primary winding to minimize the leakage flux.

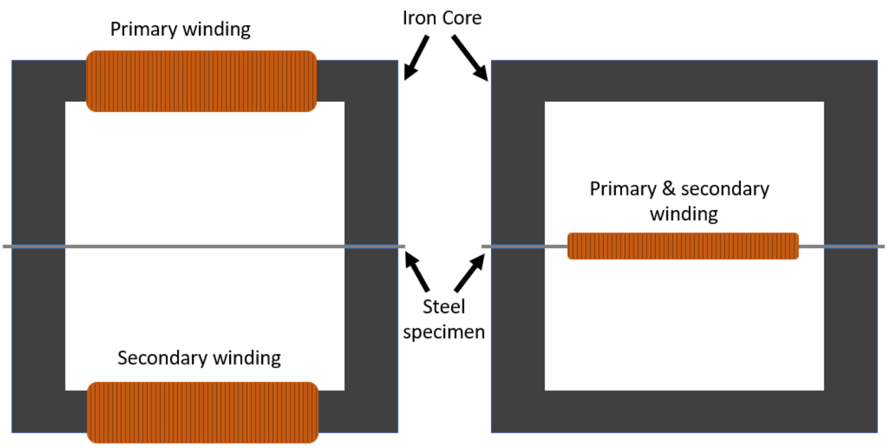

Figure 4.1: A single sheet tester can have the primary and secondary windigns wound on the top and bottom core respectively(left) or on a bobbin that surronds the sample(right).

Magnetic flux is induced in the steel sample and the two cores by applying a sinusoidal voltage to the excitation winding through Faraday´s law

$$EMF(rms) = 4.44 f N \hat{B} A \tag{4.1}$$

where EMF is the rms value of the voltage applied to the primary winding, 4.44 is the form factor considering sinusoidal flux, f is the electrical frequency of the sinusoidal voltage, N is the number of turns in the primary winding, $\hat{B}$ is the desired flux density amplitude and A is the cross sectional area of the steel sample under test.

The hysteresis characteristics of the steel sheet can be determined by measuring the voltage of the secondary winding and the current of the primary winding for different frequencies and flux densities. By using Amperes law in (2.2) together with the following expression, the magnetic flux density and the magnetic field in the steel sample can be found as

$$B(t) = \frac{1}{N_2 A} \int_0^T U_2(t) dt \tag{4.2}$$

where $B(t)$ is the magnetic flux density, N_2 is the number of turns in the secondary winding, T is the time period of the voltage waveform and $U_2(t)$ is the voltage measured at the secondary winding.

One alternate method of measuring the hysteresis characteristics using an SST utilizes a B-coil and an H-coil. The B-coil acts as an secondary winding of the setup but the length is typically much shorter and does not extend to the complete length of the bobbin. According to the IEC standards air-flux compensation is neccesary in the form of a mutual inductor for a standard SST to only evaluate the magnetic flux density in the lamination. However, this can lead to over- and under compensation of the air flux close to saturation. To avoid this it is suggested in [22] to use a shorter B-coil for the detection of the magnetic flux density and neglect the air-flux. By measuring the induced voltage over this coil and using (4.2) the flux density in the magnetic circuit can be found.

In order to determine the magnetic field one can place one additional coil close to the sample under investigation. This coil is called an H-coil and is typically created on a PCB or wound around a thin piece of insulating material to make it as slim as possible while simultaneously having a large number of turns so that it can be placed under the primary and secondary winding. By using an H-coil and B-coil placed at the center of the sample as is depicted in Figure 4.2, the measurements are less affected by the error caused by the magnetic field distortion near the ends of the excitation winding [22].

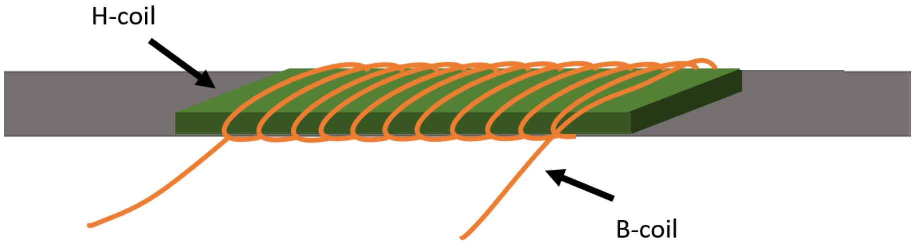

Figure 4.2: An H-coil is placed as close to the sample as possible to estimate the magnetic field inside the sample. The B-coil is wound around the sample and the H-coil.

The H-coil will have an induced voltage due to the field close to the sample and by using (4.2) and (4.1) in conjunction with the relationship between magnetic flux density and the field, the magnetic field in the sample can be estimated through

$$B = \mu_r \mu_0 H \tag{4.3}$$

where μ_r is the relative permeability, μ_0 is the permeability of vacuum and H is the magnetic field. The material in the center of the H-coil has an approximate permeability of 1 and thus (4.3) is simplified to

$$B = \mu_0 H \tag{4.4}$$

Once the magnetic flux density and the magnetic field is determined, the total specific iron loss can be calculated directly using

$$\int H dB \cdot \frac{f}{\rho} \tag{4.5}$$

where f is the electrical frequency and ρ is the mass density of the steel.

4.2 Epstein frame

In contrary to the SST the Epstein frame does not have a separate core, instead samples are positioned in a square with overlapping edges. Therefore, the number of samples required for testing with an Epstein frame is always a multiple of four. The Epstein frame has four coils where each consist of a secondary winding wound around a bobbin made of an insulating material and a primary winding winded on top of the secondary winding [23]. The four primary windings and the four secondary windings are series connected respectively as is shown in Figure 4.3.

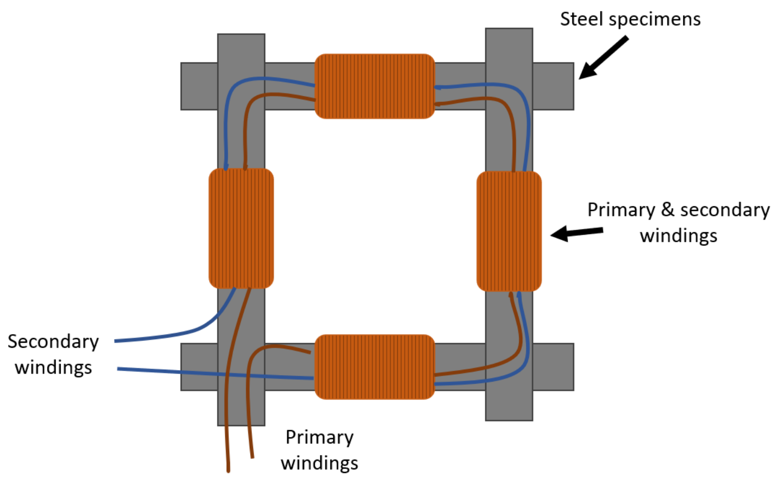

Figure 4.3: The Epstein frame use a multiple of four identical steel samples to both serve the purpose of a core and being the samples under test.

Similarly to the standard SST, the magnetic flux density is obtained from the secondary winding and (4.2). From the primary winding and (2.2) the magnetic field is found.

4.3 Toroid tester

A toroid tester, also called ring core tester, is very similar to an Epstein frame. The material under test is in the shape of a ring. The toroid tester can have both primary and secondary windings or simply the primary as is seen in Figure 4.4 [24]. Due to its shape it has a higher resemblance to machine cores compared to the SST or Epstein frame [25].

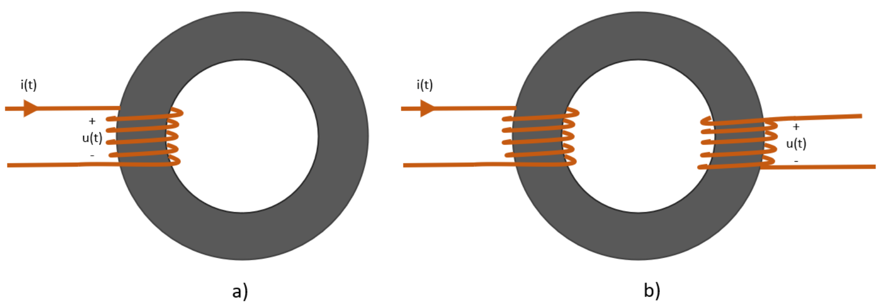

Figure 4.4: The toroid tester can have different configurations of the windings; a) only primary winding or b) both primary and secondary winding. Where the primary or secondary voltage can be used for flux density characterisation.

4.4 Rotational single sheet tester

The SST and Epstein frame presented previously does not take the rotational field into account. In order to do so an RSST can be used for measurements. The RSST can be made into different shapes where laminated yokes form a closed path with a centralized crossing point where generally a small sample is placed for investigation [26].

5

Building single sheet tester

In this thesis an SST test setup was constructed by a function generator, power amplifier, ferrite cores, windings, sensing circuits, micro-controller and a frame. In Figure 5.1 a schematic overview of the setup is presented.

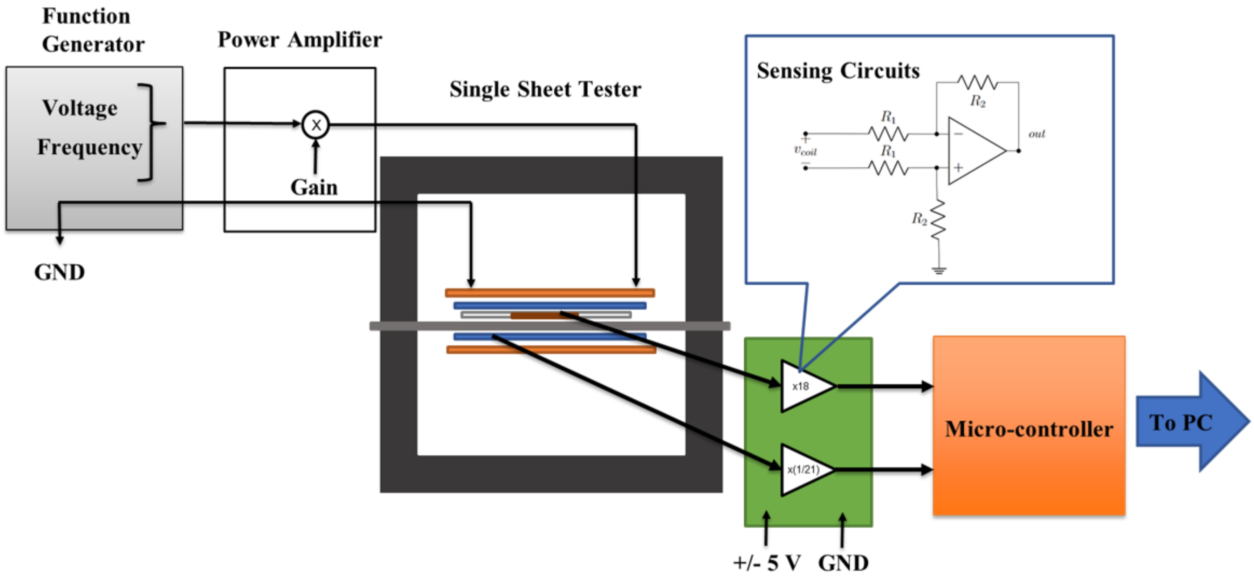

Figure 5.1: Setup overview: The single sheet tester is excited by sinusoidal voltage from a function generator in series with a power amplifier. The data is sampled by a micro-controller connected to a PC.

A function generator and a power amplifier was connected in series and then connected to the excitation winding as in Figure 5.1. From the function generator a sinusoidal voltage was generated, fed into the amplifier and then amplified through a knob on the amplifier and forwarded to the excitation winding.

5.1 Core

The two yokes of the SST was constructed from 5 I-shaped ferrite cores as in figure 5.2.

Figure 5.2: The U-shaped ferrite yokes of the SST consisted of 5 I-shaped ferrite cores. Depth in figure is 28 mm.

As mentioned in Chapter 4.1 a standard SST is constructed using laminated cores. Similarly to transformers, laminated cores are usually preferred to ferrite cores due to the insulating layers preventing circulating currents and thus they have lower eddy current losses. However, for higher frequencies (generally above 1 kHz) ferrite cores typically generate less losses due to higher resistance compared to laminated cores. Another benefit of a solid core compared to a laminated core constructed with the same material is that the saturation of the solid core would be slightly higher due to the stacking factor of the laminated core. To summarize, a ferrite core would have slightly higher losses compared to laminated core except for at operating frequencies above roughly 1 kHz where the ferrite core would be the preferred option. Based on this it was determined that due to its properties, a ferrite core could replace the typical laminated core in the SST setup.

5.2 Windings

The sample under test was placed between the two yokes and inside a bobbin that held the windings. The bobbin was designed to the full inner length of the U-shaped cores and with a center large enough to fit both a steel sample and an H-coil inside. The bobbin was designed in a CAD program and 3D-printed. The shape of the bobbin can be seen in Figure 5.3.

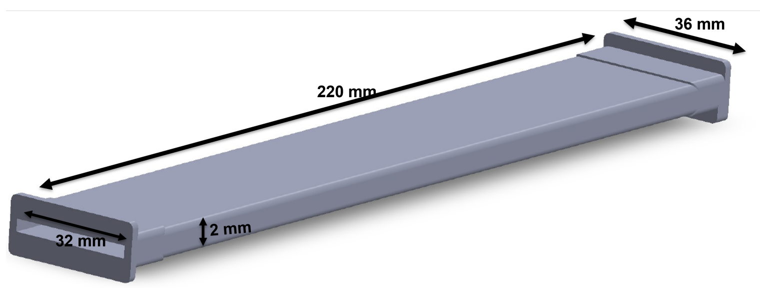

Figure 5.3: The bobbin which is required to hold the winding had to be large enough to fit both a sample and the H-coil inside.

The secondary winding was wound directly around the bobbin with a copper wire of a 0.4 mm diameter and 420 number of turns and is from now on referred to as the B-coil. The length of the B-coil was approximately set to 190 mm. The primary winding was wound with a copper winding in two layers with a diameter of 1.2 mm and a total number of 327 turns and stretched across the entire bobbin. The number of turns of the primary and secondary winding was roughly decided by using (4.1) in conjugation with the inducing voltage range of the amplifier and the desired output voltage. The diameter of the wire in the primary winding and secondary windings was decided by the estimations of the setup impedance.

5.3 H-coil

Finally an H-coil was created by winding a very thin copper wire around a thin piece of plastic with a width of 30 mm designed to rest on top of the sample inside the bobbin. The H-coil and its placement is displayed in Figure 5.4.

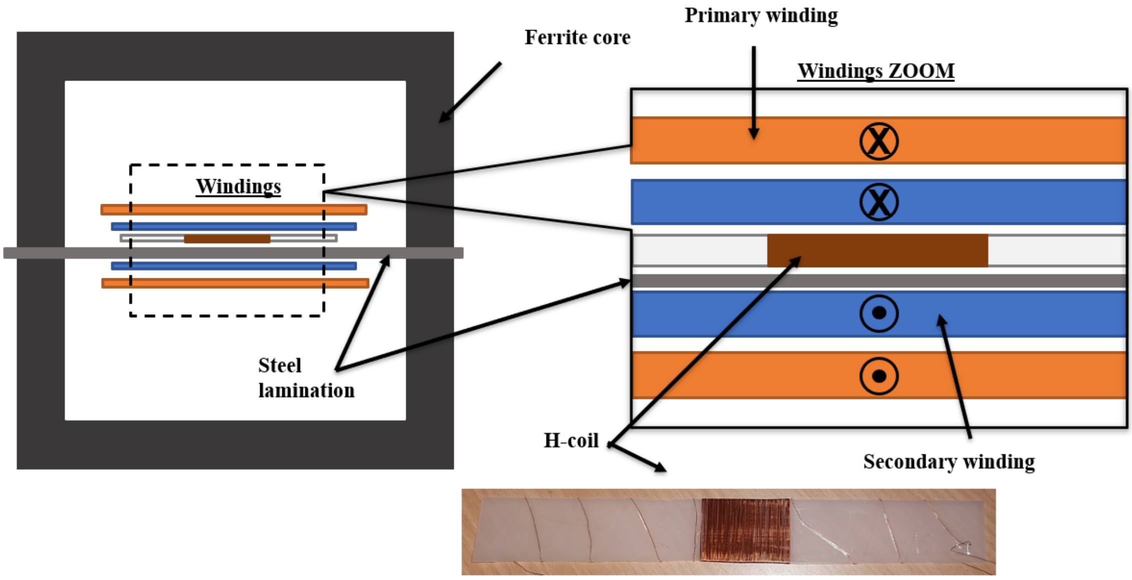

Figure 5.4: The H-coil on top of the sample inside the bobbin that holds the secondary and primary winding.

5.4 Sensing circuit

The amplitudes of the voltages over the B-coil and the H-coil was altered so that the signals could be received by a TIVA micro-controller by using amplifying circuits as presented in Figure 5.5.

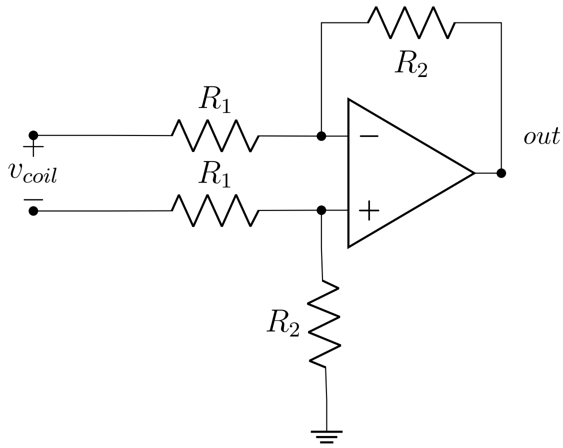

Figure 5.5: A differential amplifier with four resistors and one operational amplifier

A PCB was designed for the sensor circuits and the micro-controller as shown in Figure 5.6 where an additional sensor was added in series with a fuse to be able to receive the current from the primary winding.

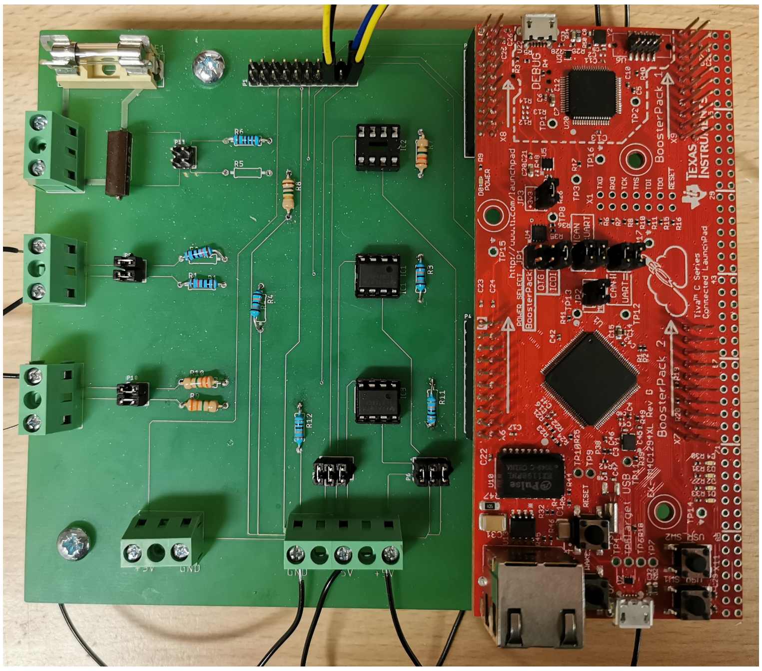

Figure 5.6: The amplifier circuits were built on a custom PCB designed with a direct mount of the micro-controller.

Furthermore the signal amplitudes were shifted to alternate around 1.65 V instead of 0 V using 9 V batteries and potentiometers to enable the micro-controller to receive the signals.

5.5 LabVIEW

Each measurement was sampled manually from the H-coil and B-coil voltage of the setup to LabVIEW. The program integrated the signals according to (4.2) to obtain the magnetic flux density. They were then recalculated corresponding to the true potentials at the coils by re-scaling the signals using the gain of the sensor circuits and the number of turns in each of the coils. The magnetic field was found by utilizing (4.4) and the total specific iron loss was found using (4.5). In Figure 5.7 an overview of the LabVIEW program is displayed.

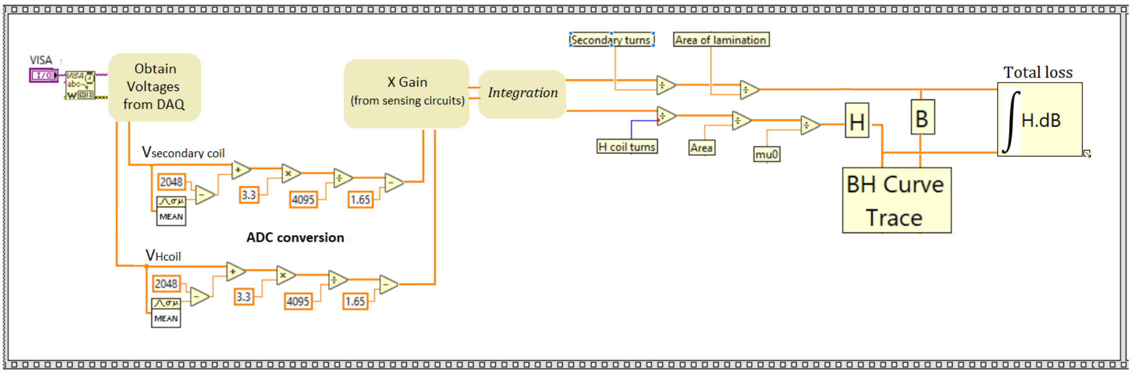

Figure 5.7: Overview of the LabVIEW program used to sample the measurement data.

5.6 Frame

In order to make the setup more robust a frame was designed using SolidWorks and then milled from a solid piece of plastic. The frame was created so that the cores could be fixed in place in order to minimize the pressure by the cores on the test specimen and the steel sample could be exchanged without removing the cores. In Figure 5.8 the SST is shown mounted inside the plastic frame.

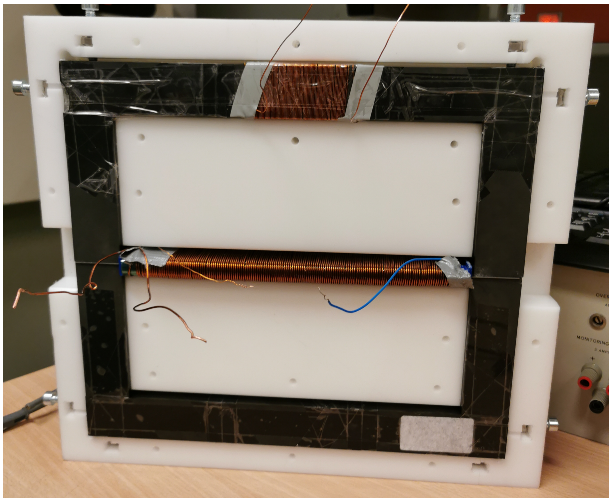

Figure 5.8: When the SST is placed inside the frame the ferrite cores can be fixed with bolts from the sides and top. The bobbin can be pulled straight out when its time to change the steel sample inside.

5.7 Steel samples

The steel laminations tested in the SST were laser cut from rectangular sheets of NO-25-1350H which is a non-oriented electrical steel with a 0.25 mm thickness [27]. The laser cutter was of type "TruLaser Cell 7040" by TRUMPF. The samples were cut to maintain the same total area and avoid the need of gluing the strips together. The strip geometries that was investigated are displayed in Figure 5.9.

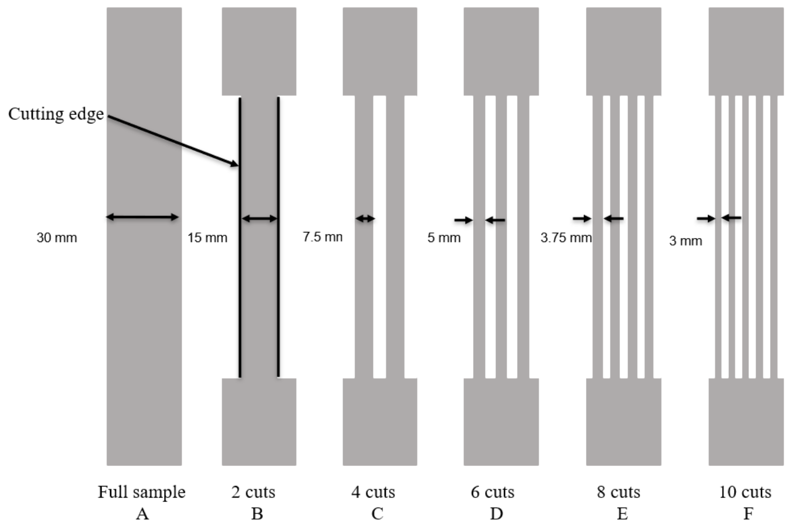

Figure 5.9: Sample A is a full dimensioned sample for the SST setup used for verification and calibration of the SST. The sample geometries B-through-F maintain the same total area and the effect of gluing is removed by cutting out air-sections in the steel strips.

The samples B through F were weighed using a scale with an accuracy of 0.01 grams to observe the loss of material. In Table 5.1 the material loss is presented for the samples with B as reference.

Table 5.1: Material loss due to cutting

Sample	**Weight [g]**	**Material loss [%]**
B	10.08	–
C	10.08	0
D	9.76	3.1
E	9.90	1.8
F	9.71	3.7

6

Verification and measurements of SST

This section describes how the setup was verified and the repeatability of the setup is presented. Further it informs how the measurements were conducted including what samples were measured, what manufacturing effects that are considered and how the data was collected. All subsequent verification tests were made at 400 Hz.

6.1 Flux compensation and leakage inductance

Flux compensation coils were made for the primary and secondary winding of the SST according to the IEC standard [21]. However there was a speculation that this coil was overcompensating the leakage flux due to a significant distortion in the secondary voltage waveform of the SST during testing. Therefore, further testing of the leakage inductance in the setup was conducted.

In general the SST can be considered to be a transformer with a primary and secondary winding. Therefore, the leakage inductance can be measured approximately with a LCR meter by short-circuiting the secondary winding. Table 6.1 shows the results of open circuit and short circuit LCR measurements of the SST with the different laminations inside.

Table 6.1: Open circuit and short circuit inductance

Sample	**Primary inductance + leakage inductance** $[mH]$	**Leakage Inductance** $[\mu H]$
A	5.25	394
B	2.00	549
C	1.51	576
D	1.41	576
E	1.39	575
F	1.34	582

In Table 6.1 it can be observed that the inductances of the circuit change with the different samples which makes flux compensation difficult. The change in the secondary voltage without flux compensation was less significant without flux compensation, thus it was discarded and the measurements were made with H-coil and B-coil.

6.2 Test of H-coil and primary winding

To confirm that the H-coil was working as expected, the received voltage from the H-coil was displayed along with the primary current for two regular test of the SST using sample A. The primary current was measured by connecting a small resistor of 0.1 Ω in series with the primary winding and a 1:1 transformer connected in parallel over the resistor for isolation purpose. In Figure 6.1 and 6.2 the waveform of the primary current is shown with the H-coil voltage and the integration of the H-coil voltage which is equivalent to the current according to Amperes Law.

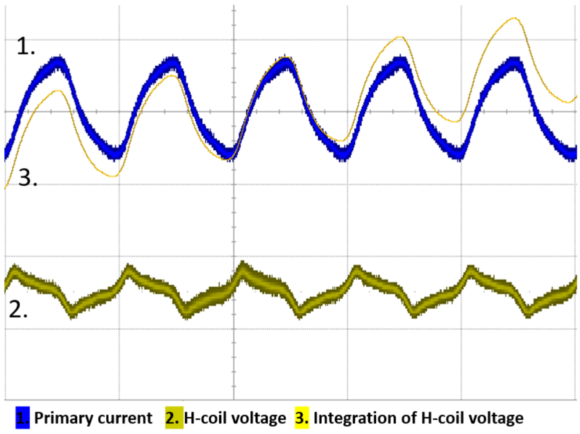

Figure 6.1: The waveforms of the current measured at the primary winding, the voltage from the H-coil and the current calculated from the H-coil at 1 T with sample A

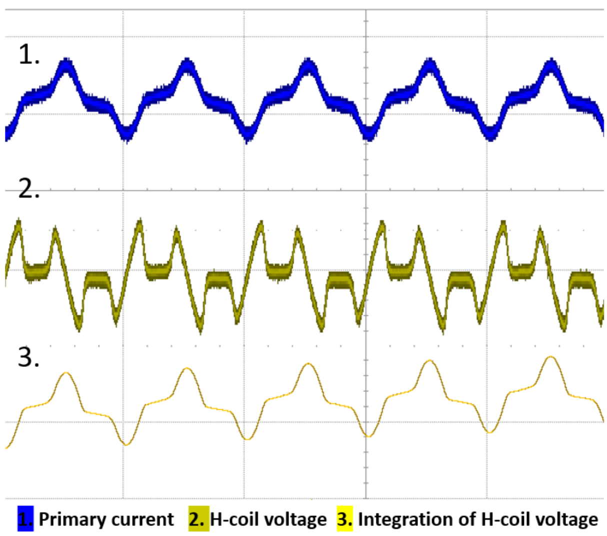

Figure 6.2: The waveforms of the current measured at the primary winding, the voltage from the H-coil and the current calculated from the H-coil at 1.5 T with sample A

From both Figure 6.1 and 6.2 it can be seen that the shape of the primary current is similar to that of the integrated H-coil voltage except for the incline of the average value of the integrated H-coil voltage. This likely occurred due to a small DC shift of the H-coil voltage and thus the incline was neglected. From the observations in this test it was found that the H-coil was working correctly.

6.3 Measurement on ferrite core

Since a standardized SST utilizies laminated iron cores, tests were made to determine the voltage in the ferrite near saturation. The cores were tested by direct excitation through a separate winding wound around the top half of the core as in Figure 6.3.

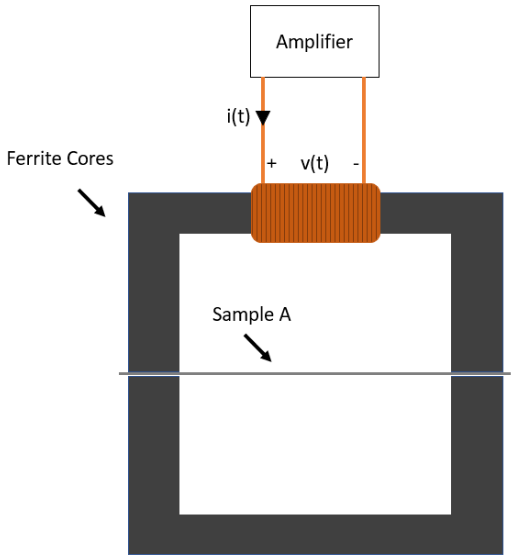

Figure 6.3: The core was tested by exciting a winding wound directly around the core.

The voltage of the amplifier was increased until the initial saturation was visible. This test was performed with and without sample A between the cores and in both cases it was found that the saturation occurred when the excitation was close to 8 V applied on the core. After this the rest of the SST setup was reconnected and the voltage in the ferrite, the primary an the secondary voltage was observed during a regular lamination test at a flux level of 1.3 T in sample A. The waveforms are presented in Figure 6.4 where the primary voltage is measured at the output of the amplifier, the core voltage is measured from the winding around the core as shown in Figure 6.3 and the secondary voltage is measured from the B-coil.

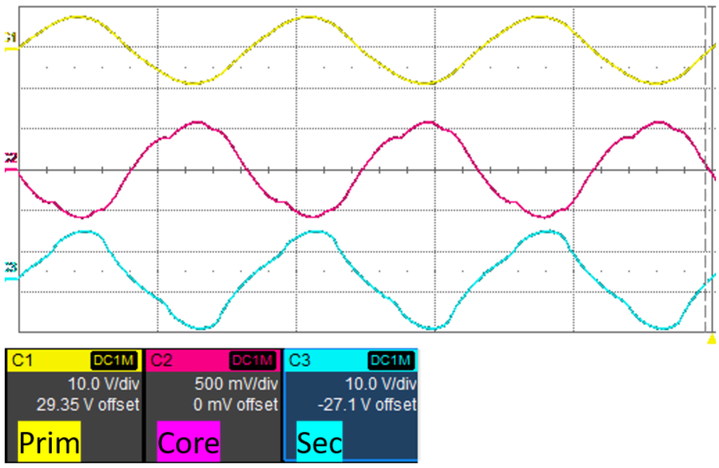

Figure 6.4: The primary voltage (Prim), the voltage measured from the winding wound around the core (Core) and the secondary voltage (Sec) measured with a flux density of approximately 1.3 T in sample A.

From Figure 6.4 it was observed that the primary voltage came through correct as a sinusoidal voltage, hence the function generator and amplifier supplied as expected. The voltage measured from the winding around the core showed some distortion due to the change in current at this flux level. In Figure 6.4 the voltage measured from the winding around the core also shows that the voltage level at this test is much lower than the initial saturation of the core. Therefore, saturation of the ferrite cores was discarded as the reason of the voltage distortion. Finally the secondary voltage show a bit of distortion at this high flux level due to that the current waveform was peaking at this level of flux density.

6.4 Measurement compared to datasheet

In order to verify the functionality of the SST setup, measurements were made with sample A and compared with the provided data in the datasheet of the steel material. The sample was excited with a range of 0.4 - 1.3 T for 400 Hz to observe the hysteresis curves along with the virgin curve from the datasheet as is depicted in Figure 6.5.

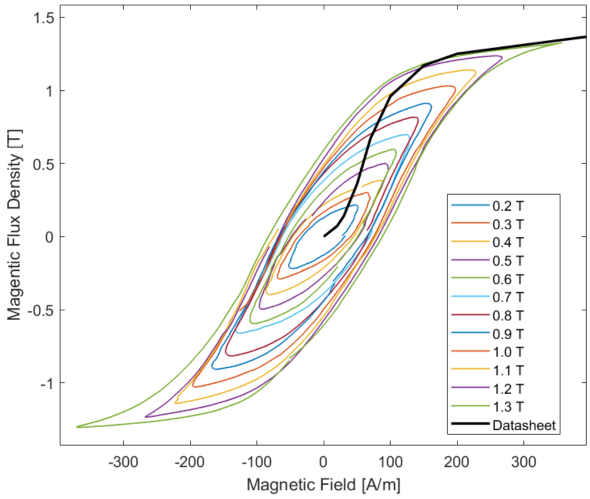

Figure 6.5: Sample A without flux compensation vs. virgin curve datasheet.

The total loss from the measurements was calculated using (2.1). To verify the accuracy of the obtained losses it was compared to the loss data from the datasheet of the material [27]. Figure 6.6 displays the losses in the datasheet along with the measured losses for 200 Hz and 400 Hz for sample A.

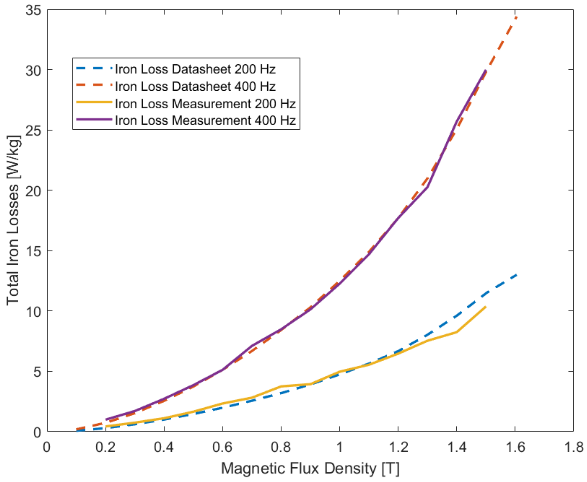

Figure 6.6: The total losses of the measurements for sample A compared to the total losses listed in the datasheet.

The maximum deviation of the measured losses was found to be 0.49 %.

6.5 Repetivity of measurements

To observe the reliability of the SST setup a repetivity test was made for a few samples at 400 Hz. The test was made for odd magnetic flux densities between 0.3 – 1.5 T. The conduction of measurements was structured from lower magnetic flux density to higher flux density. This was repeated 3 times and each time the sample was reinserted into the SST measurement setup. In Figure 6.7, 6.8 and 6.9 the repetitiveness is shown for sample A, B and C. In each figure the three tests are shown along with a curve that represents the mean value of the repetivity test.

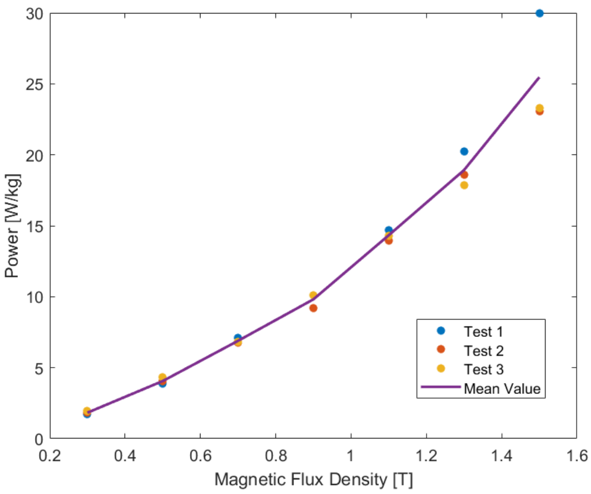

Figure 6.7: The repetitiveness of sample A displayed along with the mean value of the measurements

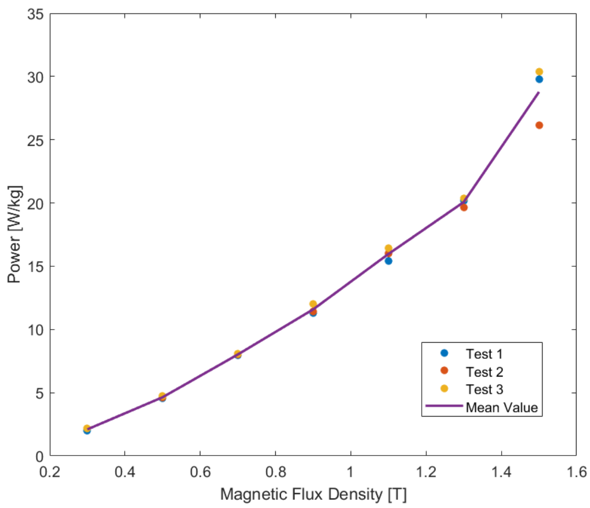

Figure 6.8: The repetitiveness of the sample B displayed along with the mean value of the measurements

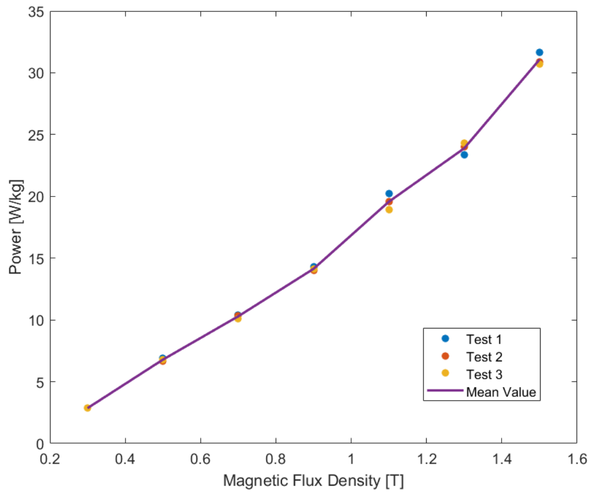

Figure 6.9: The repetitiveness of the sample C displayed along with the mean value of the measurements

From Figure 6.7-6.9 a higher deviation can be observed for higher flux densities.

6.6 Analysis of measured data

Each of the steel samples corresponds to a width from the center of the strips to the cutting edge. An example of this is shown in Figure 6.10.

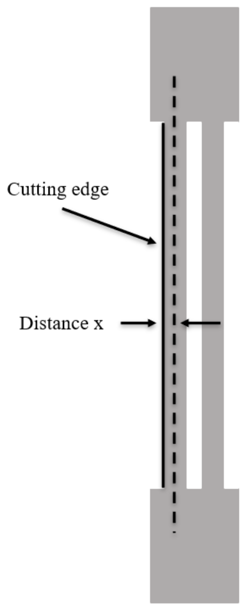

Figure 6.10: The distance x is defined as the length between the center of a solid part between two edges in each of the samples.

From this definition the distance x can be expressed as in

$$x = \frac{15}{2N_{cuts}} \tag{6.1}$$

where N_{cuts} is equal to the number of cuts in the sample. In this way each sample can be represented by its own equivalent distance x according to Table 6.2.

Table 6.2: Equivalent distance per sample

Sample	**x[mm]**
A	15
B	7.5
C	3.75
D	2.5
E	1.875
F	1.5

6.7 Measurement outline

Measurements were conducted for each sample A through F for the frequencies 200, 300, 400, 500 and 600 Hz. For each frequency the laminations were excited for a magnetic flux density range of 0.3 - 1.4 T with a step of 0.1 T.

7

Permeability and loss model and implementation in an FEM simulation

From the results obtained from the measurements, a permeability model and a iron loss model was created to be used in an FEM machine simulations for any arbitrary width of x.

7.1 Permeability model

A permeability model was derived for the obtained measurement data at 400 Hz. The purpose of creating a permeability model is to express the permeability using a function depending on H and x. A time average permeability was found for each hysteresis curve by calculating the slope of the straight line that cuts through the maximum and minimum point of the curve as depicted in Figure 7.1.

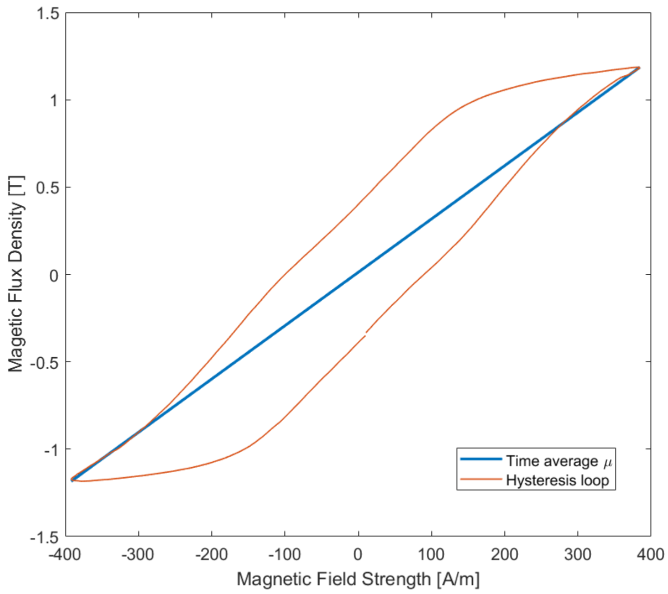

Figure 7.1: The time average of the permeability is found by calculating the slope of the straight line between the maximum and minimum point of the hysteresis curves

In order to get an expression of μ_{r-x} expressed in the magnetic field (H), polynomial curve fitting of the second degree was applied as

$$\mu_{r-x}(H) = \alpha H^3 + \beta H^2 + \gamma H + \delta \tag{7.1}$$

where α, β, γ and δ are coefficients for each lamination. At this stage five different equations are required to represent the permeability, one for each steel sample. The corresponding coefficients are listed in Appendix A.1.

To narrow it down to only one equation, polynomial curve fitting with respect to x can be applied to each of the coefficients α, β, γ and δ resulting in the following polynomials

$$\alpha(x) = \alpha_1 x^2 + \alpha_2 x + \alpha_3 \tag{7.2}$$
$$\beta(x) = \beta_1 x^2 + \beta_2 x + \beta_3 \tag{7.3}$$
$$\gamma(x) = \gamma_1 x^2 + \gamma_2 x + \gamma_3 \tag{7.4}$$
$$\delta(x) = \delta_1 x^2 + \delta_2 x + \delta_3 \tag{7.5}$$

where $\alpha(x)$, $\beta(x)$, $\gamma(x)$ and $\delta(x)$ are all changing with the distance x. The coefficients from $\alpha(x)$, $\beta(x)$, $\gamma(x)$ and $\delta(x)$ can be found in Appendix A.1.

From (7.1)-(7.5) the final expression for μ_{r-x} becomes

$$\mu_{r-x}(H, x) = \alpha(x)H^3 + \beta(x)H^2 + \gamma(x)H + \delta(x). \tag{7.6}$$

Once μ_{r-x} is known for any distance, μ_{r-x} can be used to generate virgin curves for any desired distances.

7.2 Iron loss model

To be able to model the iron losses at an arbitrary distance x from the cutting edge, Jordan's equation in (2.4) was utilized. The hysteresis and eddy current losses were separated for every measurement using the relation to frequency and then a curve fitting method was performed to each sample separately to express the relation with the magnetic flux density. Resulting expressions of $k_{hyst}(B)$, and $k_{ec}(B)$ is found as

$$k_{hyst}(B) = uB^2 + vB + w \tag{7.7}$$
$$k_{ec}(B) = pB^2 + qB + r \tag{7.8}$$

where u,v and w are coefficients for $k_{hyst}(B)$ and p, q and r are coefficients for $k_{ec}(B)$ respectively. The values for these coefficients can be found in Appendix A.2.

To model the relation with the distance x, another curve fitting process was applied to the coefficients of (7.7) and (7.8) and resulting in the following coefficient expressions

$$u(x) = u_1 x^3 + u_2 x^2 + u_3 x + u_4 \tag{7.9}$$
$$v(x) = v_1 x^3 + v_2 x^2 + v_3 x + v_4 \tag{7.10}$$
$$w(x) = w_1 x^3 + w_2 x^2 + w_3 x + w_4 \tag{7.11}$$
$$p(x) = p_1 x^3 + p_2 x^2 + p_3 x + p_4 \tag{7.12}$$
$$q(x) = q_1 x^3 + q_2 x^2 + q_3 x + q_4 \tag{7.13}$$
$$r(x) = r_1 x^3 + r_2 x^2 + r_3 x + r_4 \tag{7.14}$$

where u_x, v_x, w_x, p_x, q_x and r_x are the coefficients for the curve fit. The coefficients can be found in Appendix A.2. The iron losses can now be expressed according to

$$k_{hyst}(B, x) = u(x)B^2 + v(x)B + w(x) \tag{7.15}$$
$$k_{ec}(B, x) = p(x)B^2 + q(x)B + r(x) \tag{7.16}$$

7.3 Machine simulation

For implementation of the permeability model and the loss model a 3-phase IPM reference machine was simulated in COMSOL Multiphysics. The full geometry of the machine is shown in Figure 7.2.

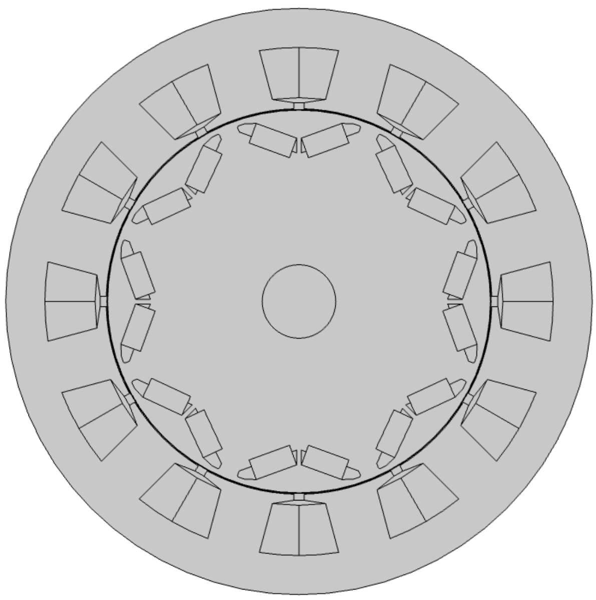

Figure 7.2: V-shaped IPM machine used for implementation of the permeability model and loss model.

The parameters of the machine are specified in Table 7.1 and the electrical ratings are shown in Table 7.2.

Table 7.1: Machine parameters

Parameter	**Value**
Stator slots	12
Poles	8
Stator outer radius	105.72 mm
Stator inner radius	69.5 mm
Rotor outer radius	69 mm
Rotor inner radius	26.5 mm
Magnet thickness	7.52 mm
Magnet width	15.5 mm
Active length	0.13 m

Table 7.2: Electrical ratings

Electrical parameters	**Value**
Input power	42.1 kW
Phase voltage (peak)	250 V
Phase current (peak)	137 A
Output power	41.0 kW
Efficiency	97.24 %
Rated speed	4000 rpm
Rated torque	97.82 Nm
Rated operating frequency	266.7 Hz

7.4 Modification of simulation

The degradation of the material was modeled in the machine by dividing the stator and rotor core into layers with separate material properties as was proposed in [7]. The layering is shown in Figure 7.3.

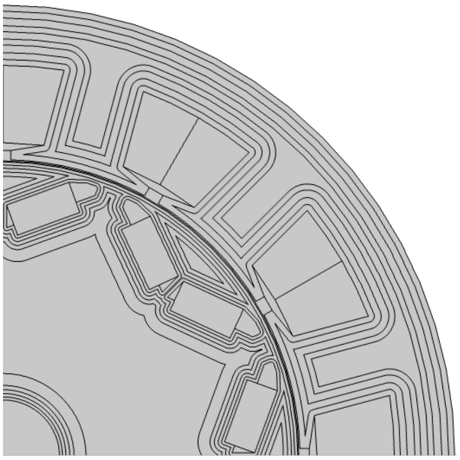

Figure 7.3: Quarter of V-shaped IPM machine with added degradation layers.

The size of the layers are presented in Table 7.3 and the equivalent distance x_s for the stator is found from t_s through

$$x_{s1} = \frac{t_{s1}}{2} \tag{7.17}$$

$$x_{s2} = t_{s1} + \frac{t_{s2}}{2} \tag{7.18}$$

$$x_{s3} = t_{s1} + t_{s2} + \frac{t_{s3}}{2} \tag{7.19}$$

$$x_{s4} = t_{s1} + t_{s2} + t_{s3} + \frac{t_{s4}}{2} \tag{7.20}$$

$$\tag{7.21}$$

where x_{s1}, x_{s2}, x_{s3}, x_{s4} are the equivalent distance of the layers in the stator from the laminations outer edge and t_{s1}, t_{s2}, t_{s3}, t_{s4} are the actual thickness of the layers. The rotor equivalent distance of the rotor layers are found in the same manner.

Table 7.3: Layering of IPM machine

Layer	**Thickness t [mm]**	**Equivalent distance x [mm]**
Stator 1	1.4	0.7
Stator 2	1.6	2.2
Stator 3	1.8	3.9
Stator 4	1.4	5.5
Rotor 1	0.7	0.35
Rotor 2	0.8	1.1
Rotor 3	0.9	1.95
Rotor 4	1	2.9
Rotor 5	2.8	4.8

For the remaining yoke of the stator and rotor the material was set to the material specified in the datasheet of the steel material [27]. The equivalent x value was then used to generate an individual virgin curve for each layer to define the material in COMSOL. The same x parameter was also used to define the hysteresis and eddy current coefficients used in the loss determination. This was inserted as a user defined loss model for each core layer in COMSOL.

To quantify the results of the simulation, the same machine model was used with every layer having the material specified by the virgin curve presented in the datasheet. The machine was simulated at the rated speed for full load and 75 % load using current excitation.

8

Results

This chapter includes the results from the permeability model, the loss model and the FEM simulation of the IPM machine.

8.1 Measurements

From the measurements the relation for different samples and different levels of flux density could be observed as in Figure 8.1.

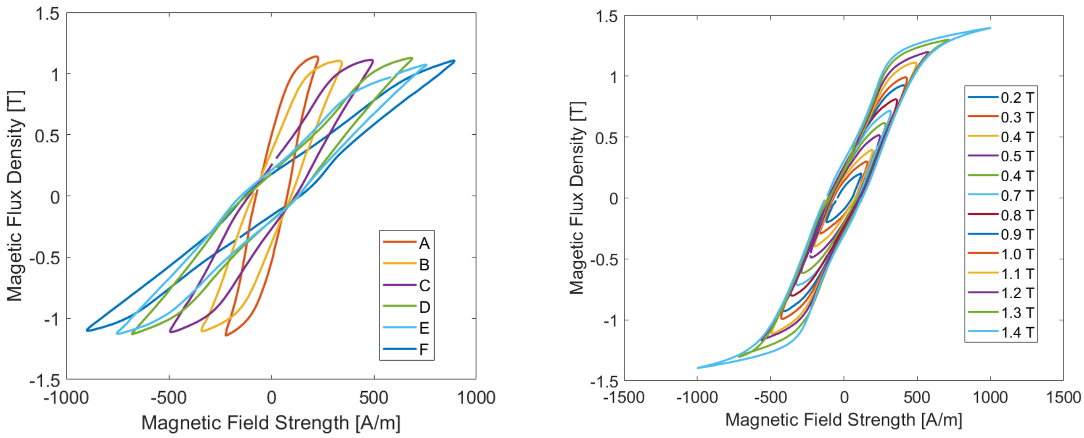

(a) Hysteresis loops for A-F at 1.1 T. **(b)** Hysteresis loops for sample C.

Figure 8.1: The change in hysteresis loops for the different samples and flux levels.

From the measurements of different samples, a decrease in permeability was noticed for decreasing equivalent distance x to the cutting edge as is shown in Figure 8.1a. In Figure 8.1b it can be seen how the area of the hysteresis loops increase with increasing flux density in sample C. The hysteresis loops for all samples at the ranges of 0.2 - 1.4 T at 200, 300, 400, 500, and 600 Hz can be found in Appendix A.3.

8.2 Permeability

In Figure 8.2 the change of the time average permeability between the tests are displayed. In Figure 8.2a the slopes are displayed with respect to lamination samples for 1.1 T. In Figure 8.2b the slope of the permeability can be seen for sample C for different values of magnetic flux density.

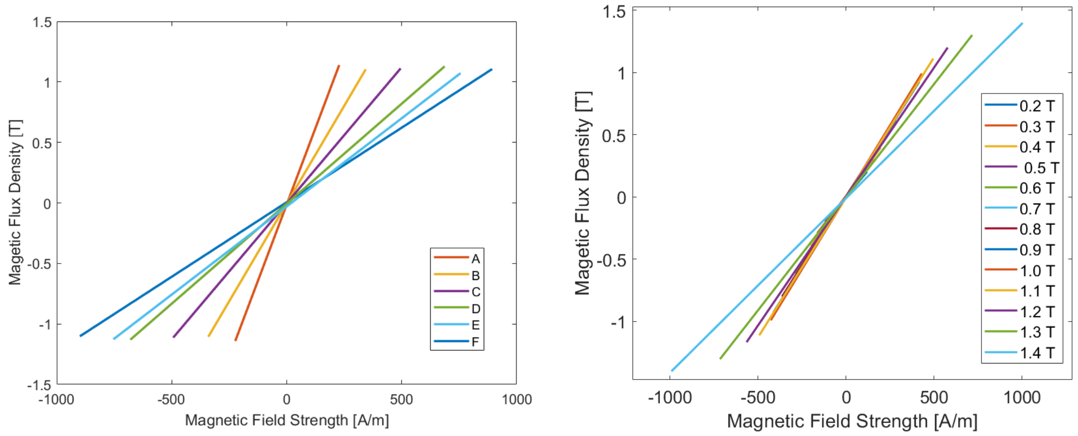

(a) Change in permeability for A-F

(b) Change in permeability for sample C.

Figure 8.2: The permeability decrease with increasing flux density and with the decreasing width x.

From Figure 8.2a and 8.2bit was observed that the time average permeability decrease with decreasing equivalent distance x and increasing flux density. From the resulting permeability, the virgin curves could be sketched for each sample. These curves are shown in Figure 8.3.

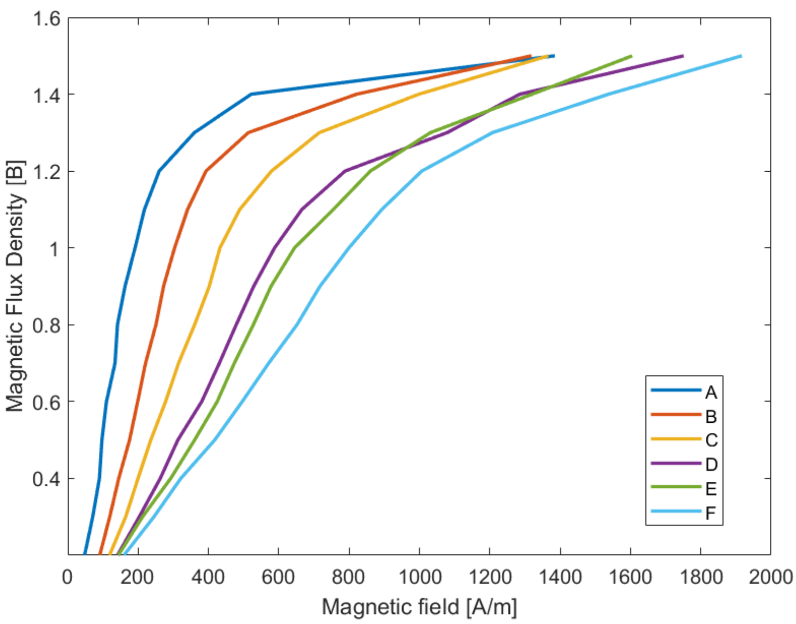

Figure 8.3: From the time average permeability found for all measurement points on each sample, virgin curves could be sketched for sample A to F.

Table 8.1 shows the average deviation from sample A expressed in percent.

Table 8.1: Permeability deviation

Sample	Deviation from sample A[%]
B	11.57
C	17.70
D	24.00
E	25.03
F	29.28

Using (4.3) we can calculate the relative permeability in the steel samples for the selected values of the magnetic field. In Figure 8.4 the relation between the relative permeability and magnetic field is shown.

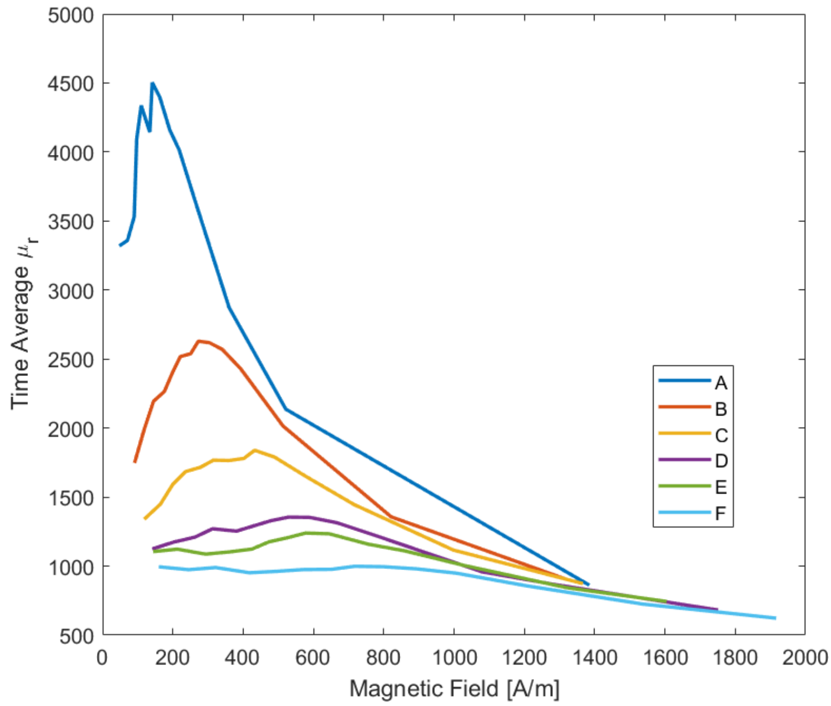

Figure 8.4: The relative permeability decrease for all samples with increasing magnetic field.

Curve fitting was applied using (7.2)-(7.4) and (7.6). Figure 8.5 shows the results of the curve fitting procedure up until 1000 A/m.

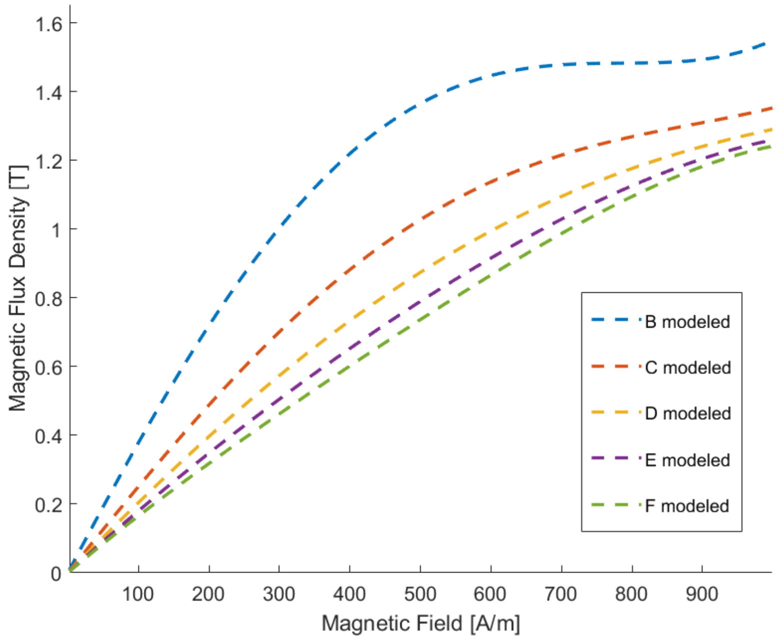

Figure 8.5: The modeled virgin curves for sample B through F for magnetic field up to 1000 A/m

The mean error between the measured virgin curves in Figure 8.3 and the modeled curves in Figure 8.5 was calculated for each sample. For magnetic field up to 1000 A/m the error was found as 10 %.

In Figure 8.6 this method has been used to generate virgin curves for sample E and F.

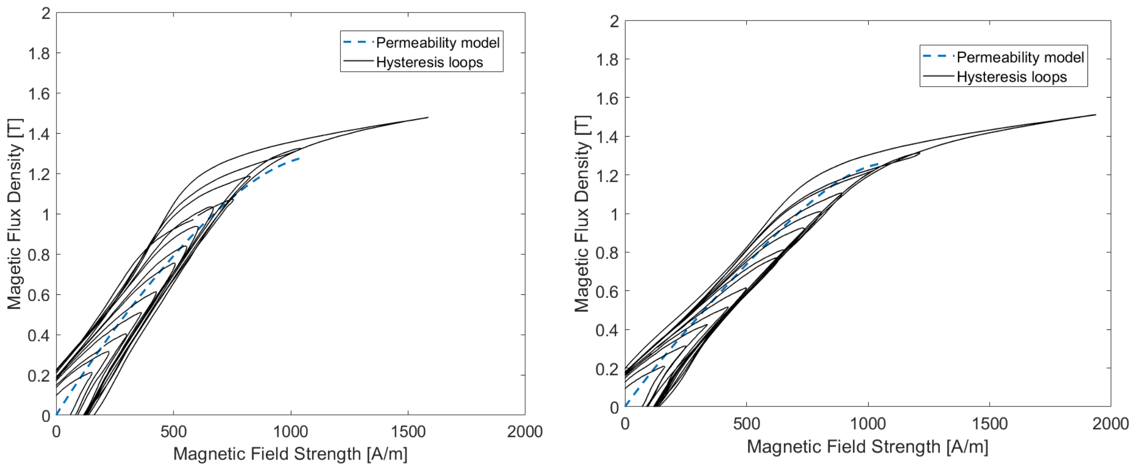

(a) Sample E **(b)** Sample F

Figure 8.6: The modeled virgin curves along with measured hysteresis loops for the corresponding sample.

8.3 Iron losses

From each hysteresis loop the total iron loss was calculated. In Figure 8.7 the relation between the width x, frequency and magnetic flux density can be observed.

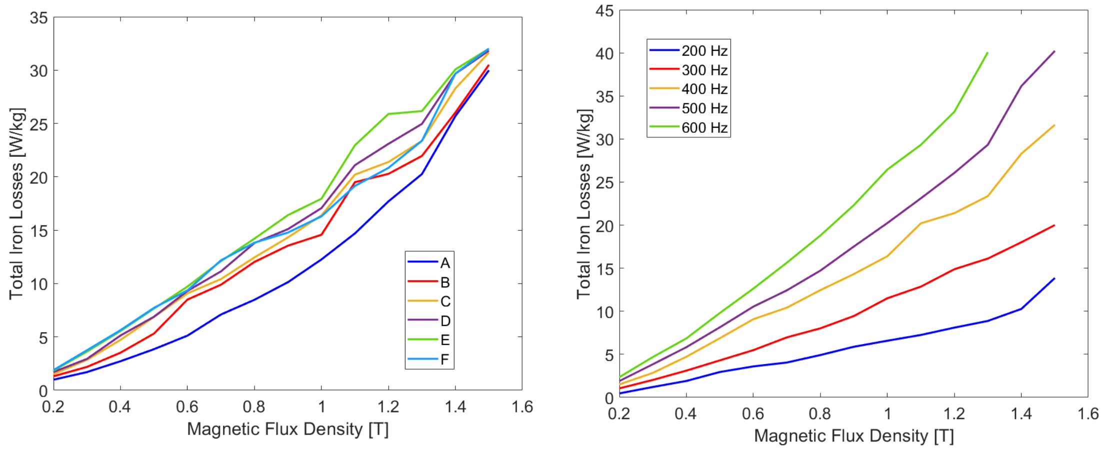

(a) Iron loss at 400 Hz sample A-F

(b) Iron loss at all frequencies sample C

Figure 8.7: The change in iron losses due to sample width and frequency

The loss coefficients k_e and k_h was found using (2.4) and the relation with frequency for each sample as seen in Figure 8.7b. In Figure 8.8 the resulting k_e and k_h is shown for all samples with changing flux density.

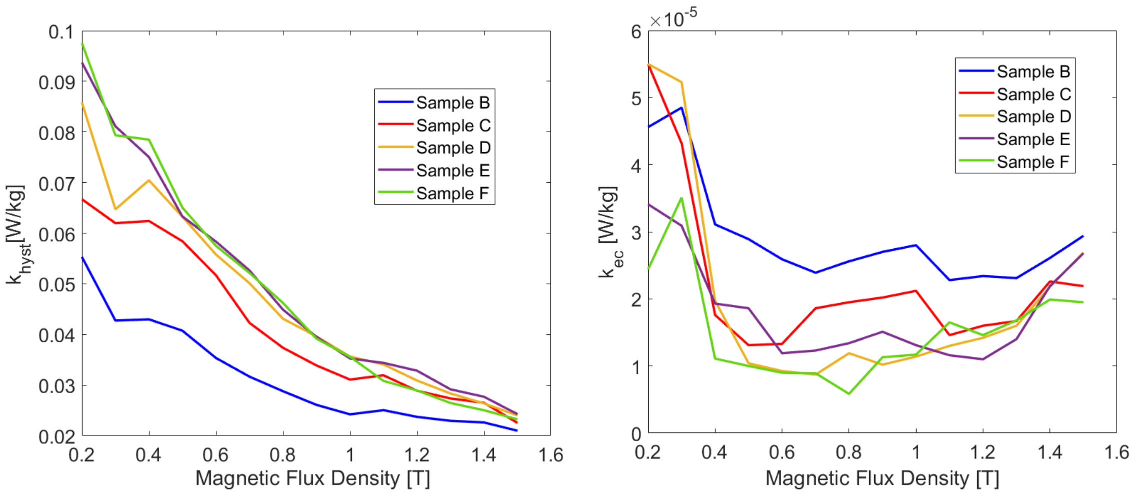

(a) Hysteresis coefficient

(b) Eddy current coefficient

Figure 8.8: The loss coefficients for Jordan's loss formula for sample B-F for different values of flux density.

From Figure 8.8a it can be seen that the hysteresis coefficient increase with a decreased equivalent distance x. Which means that the hysteresis coefficient increase closer to the cutting edge of the sample. In Figure 8.8b the opposite behaviour is observed. The calculated eddy current coefficient decrease when the equivalent distance x decrease. The total iron loss was calculated for sample C using (7.15) and (7.16) and compared to the measured iron loss which is displayed in Figure 8.9.

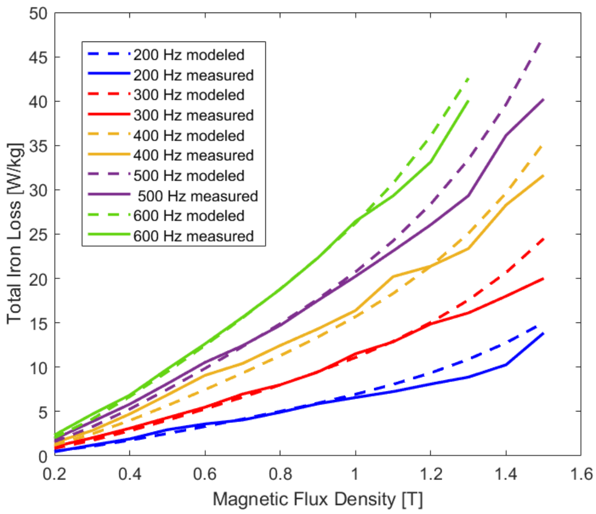

Figure 8.9: The modeled iron losses (dashed) and the measured iron losses for sample C for all frequncies.

The mean error was found for every sample and frequency as 7 %.

8.4 Simulation of IPM machine

From the simulation of the reference machine and the degraded machine, a change in flux density distribution was noticed. This change was most prominent in the teeth of the stator as can be seen in Figure 8.10.

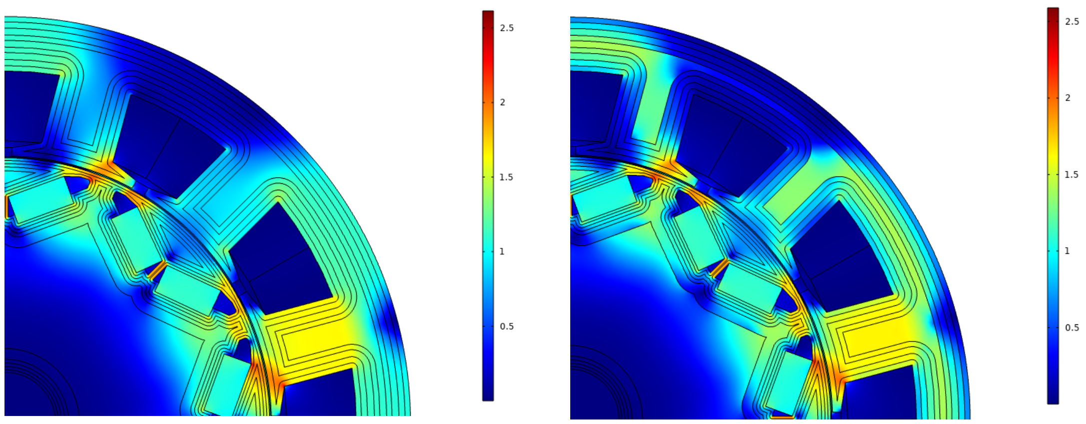

(a) Reference machine

(b) Degraded machine

Figure 8.10: Flux density distribution for full load operating point at same time instant.

The magnitude of the flux density was found higher in the center of the teeth of the degraded machine compared to the reference machine. This was expected since the permeability is lower in the degradation layers at the edges compared to the center of the yoke according to the model. Simultaneously for the stator tooth subjected to higher flux there was no visible change in flux distribution. This agreed with the permeability trend in Figure 8.4 where it could be seen that the permeability due to degradation was higher for lower fields and converged towards the same value for higher fields.

From the simulation, the iron losses were found for the two machines which is presented in terms of hysteresis losses and eddy current losses for the stator and rotor in Table 8.2 and 8.3.

Table 8.2: 100 % load

Parameter	Non-degraded	Degradation model	% Deviation
Torque	97.62 Nm	95.65 Nm	-2.01
Stator eddy current loss	293 W	195 W	-33.45
Stator hysteresis loss	575 W	760 W	+32.17
Stator total loss	868 W	955 W	+10.02
Rotor eddy current loss	138 W	75 W	-45.66
Rotor hysteresis loss	273 W	431 W	+57.88
Rotor total loss	411 W	506 W	+23.11
Total eddy current loss	431 W	270 W	-37.36
Total hysteresis loss	848 W	1191 W	+40.45
Total iron loss	1279 W	1461 W	+14.23
Efficiency %	96.97 W	96.48 W	-0.49

Table 8.3: 75 % load

Parameter	Non-degraded	Degradation model	% Deviation
Torque	72.42 Nm	70.28 Nm	-2.95
Stator eddy current loss	254 W	161 W	-36.61
Stator hysteresis loss	499 W	705 W	+41.28
Stator total loss	753 W	866 W	+15.01
Rotor eddy current loss	132 W	66 W	-50.00
Rotor hysteresis loss	259 W	410 W	+58.30
Rotor total loss	391 W	476 W	+21.74
Total eddy current loss	386 W	227 W	-41.19
Total hysteresis loss	758 W	1115 W	+47.10
Total iron loss	1144 W	1342 W	+17.31
Efficiency %	96.37 W	95.64 W	-0.37

From the losses in Table 8.2 and 8.3 it can be seen that the two operating point resulted in a similar loss deviation. In both cases the hysteresis losses increased significantly, which aligns well with what was observed in Figure 8.8a. Additionally a decrease is observed in the eddy current losses that could be traced back to the decrease of the eddy current loss coefficient observed in 8.8b. A small decrease in torque and efficiency can also be observed for both cases.

9
Discussion

9.1 Single sheet tester

No flux compensation was used with the SST due to varying leakage inductance because of the changing geometry of the samples and the utilization of an H-coil and a B-coil. Thus the leakage air-flux was neglected. According to [28] the SST requires calibration with either an Epstein frame or a toroid tester, neither of which has been conducted in this thesis due to that no such setup was available, and it was out of the scope of this thesis to build a complete Epstein frame or toroid tester.

9.2 Steel samples

It has not been thoroughly studied how the air-gaps in the sample geometries effect the flux distribution in the specimens and the air-flux of the setup. In this project an assumption was made that the cross section area was the thickness of the sample multiplied with the total width of active material e.g. 0.25 x 15 mm. This theory appeared to be true for flux densities lower than 0.7 T and sample B and C. For higher flux densities and sample D-F this was no longer a good estimation. A comparative analysis could be made with the sheet geometry presented in this thesis compared to the standard approach of strip measurements as in [8]. Samples with this type of geometry was obtained for the thesis but due to time limitations the comparison was not conducted.

The design of the samples used in this thesis was made with the motivation that no material would be lost in the cutting process. To confirm this the samples were weighted and a change in weight was noticed. This change in weight reflects a change in material that could contribute to the observed change in inductance.

9.3 Measurements

While comparing the measurements of steel specimens used in this project with the data in the steel datasheet it should be remembered that the data from the datasheet is measured on a sample that is as close to ideal as possible. Even while treated with care, the samples in this thesis has been cut with a laser cutter, handled numerous times, corrosion might be occurring at the edges, scratches might have occurred while inserting the sample in the setup and mechanical stresses might have been applied at occasions. Therefore the results from the measurements are not expected to align with the datasheet completely and thus can not be be used for a accurate calibration. However, it could be used as an indication that the results were within a reasonable range.

While testing the repetivity of the setup it was discovered that it was poorer for higher flux densities. This can be explained by the high saturation. For a small change in magnetic flux density the losses will change a lot. Therefore, with a setup that is manually operated, it is very difficult to get a high repeatability for higher flux densities.

9.4 Permeability and loss models

The permeability model is only derived for the measurements taken at 400 Hz but since the permeability of the material does not change with frequency, this model is ideally valid for the whole frequency range. Similarly, the relation with frequency and iron losses is taken care of in the iron loss expression of Jordan's equation in (2.4). Therefore, the hysteresis coefficient and the eddy current coefficient has no relation to frequency and thus they can be used for any frequency desired.

From Figure 8.5 and 8.6 it can be seen that for a magnetic field higher than 1000 A/m the model becomes quite poor for sample B and yields an error above 10 % which was deemed the acceptable maximum error for this thesis. For the machine simulation model the obtained virgin curves was extrapolated in COMSOL from the flux at 4.5e+6 A/m to a magnetic flux density of 8 T. Additionally sample B corresponds to a width x of 7.5 mm, which is significantly wider than the widths used in the machine model. Undoubtedly, the model works best under limited constraints of distance x and magnetic field.

The poor approximation of the permeability for a field above 1000 A/m could be related to the difficulty of taking measurements at higher flux density due to poor repeatability. Additionally the error in the permeability model could be induced by the difficulty of taking measurements at lower flux density due to the very low required input voltage. However, the main reason found for the discrepancy in permeability originated at an interpolation of the measured data which was necessary due to too few measurement points for a decent model fit at lower fields.

9.5 Machine simulation

In the simulated machines the layers of the rotor were made finer compared to the stator because of the geometry of the machine. A test was made with rotor layers with the same depth as those in the stator, however this yielded a large increase in eddy current losses and a minor increase in hysteresis losses. The reason for this is unknown but a theory is that the layers were too coarse to properly model the degradation in the bridges above the magnets, therefore the layers were made finer in the rotor. The result from this simulation agreed more with the expected results which is a significant change in hysteresis loss due to degradation. Further it can be seen in Table 8.2 that the eddy current loss decreased in the stator and rotor with degradation model and while it is not known why this occurs if could be related to the lowered flux density in the degradation layers. Additionally from Figure 8.8 it is visible that the hysteresis coefficient increase closer to the cutting edge while the eddy current coefficient decrease. From this it was observed that the model was sensitive to the size of the degradation layers. This behaviour was expected since each layer is defined with the material properties calculated for the center of the layer. This means that too large layers would severely underestimate the change in permeability and loss at the outermost edge and underestimate it at the innermost edge.

While comparing the results of the machines it is important to remember the different factors that could be contributing to the difference in losses except for the deterioration due to laser cutting. Possible factors are contamination of steel specimens, air-flux effect due to the geometry of the samples, loss of material in the samples, repeatability and quality of measurement setup and finally the error factor of the derived mathematical models.

Only a few operating points were studied in this report since the iron loss expressions implemented in COMSOL depend on the varying flux. This made the computation of the models comparatively slow and therefore generating a sweep of i_d and i_q currents would not have been realistic in the time frame of the project.

It should also be taken into consideration that the loss equations are based on the assumption that the magnetic flux density is sinusoidal and thus the SST ideally requires a sinusoidal flux, the flux density in an electrical machine is rarely sinusoidal.

9.6 Ethics & sustainability

Even though the vehicle industry is steadily converting from combustion engines to electrical motors there will always be a requirement to construct vehicles with as efficient components as possible. By including manufacturing defects in the simulation stage, more efficient machines can be constructed and while this might reduce the environmental cost of the construction stage, it could also lead to more efficient machines on the market.

A risk of discretizing the manufacturing processes through mathematical models is that the model of the degradation might be over- or underestimating depending on how inclusive the model is made. There are more processes than cutting and joining of the steel samples that should be considered when constructing EM cores. For instance there are processes which can be applied that are mitigating the degradation of the steel such as annealing. In this project only laser cutting was considered as a manufacturing defect. This is not representable as a complete machine core and thus the results of the simulations in this thesis should be studied with caution.

10
Conclusions

The aim of this thesis was to investigate how a manufacturing method could deteriorate the magnetic properties of steel sheets used for machine manufacturing. Further the aim was to derive a model of these deteriorations that could be implemented in an FEM simulation model of an EM.

During the first part of this thesis an SST setup was constructed and its functionality was verified with the information in the datasheet of the steel laminations. Measurements were taken for a few different samples, each with different widths between cuts, a range of frequencies and for magnetic flux densities up to roughly 1.5 T. For EM FEM simulations in COMSOL two mathematical models were created; one permeability model to generate virgin curves and one to generate hysteresis and eddy current coefficients for arbitrary deterioration depths. The average error for the permeability model was found to be 10 % and for the iron loss model it was 7 %. The results of the FEM simulations showed a potential of including the manufacturing defects in the simulation stage. There was a significant change in iron losses between the machine with and without deterioration model. The machine simulation yielded a 40.45 % increase in hysteresis losses and 37.36 % decrease in eddy current losses for full load operation. For 75 % load operation the results were similair with a 47.10 % increase in hysteresis losses and a 41.19 % decrease in eddy current losses. These changes might be enhanced by the error in the models, originating in poor measurement results. To conclude, a promising modelling method of manufacturing deterioration in an EM in COMSOL has been tested and further work with a reliable measuring setup is suggested for less discrepancies in the permeability and iron loss models.

Iron losses is a challenging topic where the interest has increased significantly the last few years. For future development of model implementation for defects caused by manufacturing in FEM simulations it would be interesting to include other manufacturing defects such as other cutting techniques, joining techniques and even annealing effects.

For future development of the specific project described in this report a proper calibration of the SST would be recommended or directly using a reliable test setup for new measurements. The alternatives for flux compensation can also be investigated further for measurements of higher accuracy especially at higher flux densities. A thorough study should be conducted on samples with different geometries using a reliable test setup to observe the effects of the air-sections in the samples in this thesis. Furthermore, the steel type could be tested using a RSST to include the rotational losses for a better approximation of the physics inside an EM. The permeability model and the models for the loss coefficients in this report is modeled strictly using polynomial curve fitting. An investigation could be made to find a more appropriate way of modeling the magnetic properties of the machine core material. The separation of the losses could be made with a more inclusive loss model compared to Jordan's equation, for a more detailed loss derivation. Additionally the simulation could be conducted at more operating points using voltage excitation and be tested on other machine designs.

Bibliography

[1] M. Villalon, "Comparative analysis between glue fastec®, conventional fastenings and housing compression effect in electric motor core losses," Nov. 2020.

[2] I. Gürbüz, F. Martin, U. Aydin, *et al.*, "Experimental characterization of the effect of uniaxial stress on magnetization and iron losses of electrical steel sheets cut by punching process," *Journal of Magnetism and Magnetic Materials*, vol. 549, p. 168 983, 2022, ISSN: 0304-8853. DOI: `https://doi.org/10.1016/j.jmmm.2021.168983`. [Online]. Available: `https://www.sciencedirect.com/science/article/pii/S030488532101177X`.

[3] Ş. Bayraktar and Y. Turgut, "Effects of different cutting methods for electrical steel sheets on performance of induction motors," *Proceedings of the Institution of Mechanical Engineers Part B Journal of Engineering Manufacture*, vol. 232, pp. 1287–1294, Aug. 2016. DOI: `10.1177/0954405416666899`.

[4] W. M. Arshad, T. Ryckebush, F. Magnussen, *et al.*, "Incorporating lamination processing and component manufacturing in electrical machine design tools," in *2007 IEEE Industry Applications Annual Meeting*, 2007, pp. 94–102. DOI: `10.1109/07IAS.2007.21`.

[5] M. Bali and A. Muetze, "The degradation depth of electrical steel sheets due to mechanical and laser cutting," in *2017 IEEE 11th International Symposium on Diagnostics for Electrical Machines, Power Electronics and Drives (SDEMPED)*, 2017, pp. 544–549. DOI: `10.1109/DEMPED.2017.8062408`.

[6] ——, "Modeling the effect of cutting on the magnetic properties of electrical steel sheets," *IEEE Transactions on Industrial Electronics*, vol. 64, no. 3, pp. 2547–2556, 2017. DOI: `10.1109/TIE.2016.2589920`.

[7] M. Bali, H. De Gersem, and A. Muetze, "Finite-element modeling of magnetic material degradation due to punching," *IEEE Transactions on Magnetics*, vol. 50, no. 2, pp. 745–748, 2014. DOI: `10.1109/TMAG.2013.2283967`.

[8] R. Sundaria, D. G. Nair, A. Lehikoinen, A. Arkkio, and A. Belahcen, "Effect of laser cutting on core losses in electrical machines—measurements and modeling," *IEEE Transactions on Industrial Electronics*, vol. 67, no. 9, pp. 7354–7363, 2020. DOI: `10.1109/TIE.2019.2942564`.

[9] Z.-Q. Zhu, S. Xue, W. Chu, *et al.*, "Evaluation of iron loss models in electrical machines," *IEEE Transactions on Industry Applications*, vol. 55, pp. 1461–1472, 2019, Accessed on: Mar 07, 2022. [Online]. Available: `https://ieeexplore.ieee.org/document/8531734`.

[10] W. M. Saslow, *Electricity, Magnetism, and Light*. Academic Press, 2002, ch. Chapter 13 - Mechanical Implications of Faraday's Law: Motors and Generators.

[Online]. Available: https://doi.org/10.1016/B978-012619455-5.50013-9.

[11] G. P. Shultz, *Transformers and Motors*. Newnes, 1989, ch. Chapter 1 - Fundamental Concepts: Transformers. [Online]. Available: https://doi.org/10.1016/B978-0-08-051958-6.50004-4.

[12] A. Krings and J. Soulard, "Overview and comparison of iron loss models for electrical machines. journal of electrical engineering," *Journal of Electrical Engineering*, vol. 10, pp. 162–169, 2010, Accessed on: Mar 07, 2022. [Online]. Available: https://www.researchgate.net/publication/228490936_Overview_and_Comparison_of_Iron_Loss_Models_for_Electrical_Machines/stats.

[13] X. Lv, D. Sun, and L. Sun, "Determination of iron loss coefficients of ferromagnetic materials used in cryogenic motors," in *2019 22nd International Conference on Electrical Machines and Systems (ICEMS)*, 2019, pp. 1–5. DOI: 10.1109/ICEMS.2019.8922160.

[14] G. Bertotti, "Physical interpretation of eddy current losses in ferromagnetic materials. i. theoretical considerations," *Journal of Applied Physics*, vol. 57, no. 6, pp. 2110–2117, 1985. [Online]. Available: https://doi.org/10.1063/1.334404.

[15] N. Stranges and R. Findlay, "Measurement of rotational iron losses in electrical sheet," *IEEE Transactions on Magnetics*, vol. 36, no. 5, pp. 3457–3459, 2000. DOI: 10.1109/20.908859.

[16] S. Jacobs, D. Hectors, F. Henrotte, *et al.*, "Magnetic material optimization for hybrid vehicle pmsm drives," *World Electric Vehicle Journal*, vol. 3, Dec. 2009. DOI: 10.3390/wevj3040875.

[17] R. BILLARDON, L. HIRSINGER, and F. OSSART, "Section 9.16 - elasticity coupled with magnetism," in *Handbook of Materials Behavior Models*, J. LEMAITRE, Ed., Burlington: Academic Press, 2001, pp. 928–943, ISBN: 978-0-12-443341-0. DOI: https://doi.org/10.1016/B978-012443341-0/50095-8. [Online]. Available: https://www.sciencedirect.com/science/article/pii/B9780124433410500958.

[18] A. Benabou, S. Clénet, and F. Piriou, "Comparison of preisach and jiles–atherton models to take into account hysteresis phenomenon for finite element analysis," *Journal of Magnetism and Magnetic Materials*, vol. 261, no. 1, pp. 139–160, 2003, ISSN: 0304-8853. DOI: https://doi.org/10.1016/S0304-8853(02)01463-4. [Online]. Available: https://www.sciencedirect.com/science/article/pii/S0304885302014634.

[19] Y. Kurosaki, H. Mogi, H. Fujii, T. Kubota, and M. Shiozaki, "Importance of punching and workability in non-oriented electrical steel sheets," *Journal of Magnetism and Magnetic Materials*, vol. 320, pp. 2474–2480, 2008, Accessed on: May 09, 2022. [Online]. Available: https://doi.org/10.1016/j.jmmm.2008.04.073.

[20] C. Xia, H. Wang, Y. Wu, and H. Wang, "Joining of the laminated electrical steels in motor manufacturing: A review," *Materials*, vol. 13, Oct. 2020. DOI: 10.3390/ma13204583.

[21] IEC, *60404-3: Magnetic materials- part 3: Methods of measurement of the magnetic properties of electrical steel strip and sheet by means of a single sheet tester*. 2010.

[22] Q. Tang, P. Anderson, Z. Wang, A. Moses, and P. Jarman, “Measurement of magnetic properties of electrical steels at high flux densities using an improved single sheet tester,” Jan. 2013. DOI: 10.13140/2.1.5025.5046.

[23] B. Koprivica, A. Milovanovic, and M. Plazinić, “Standard methods of measurement of the magnetic properties of electrical steel strip and sheet,” Nov. 2012.

[24] C. Wei, H. Jiannong, and Y. Xiangdong, “Novel accurate core loss test method for powder core materials in power electronics conversion,” in *2013 4th IEEE International Symposium on Power Electronics for Distributed Generation Systems (PEDG)*, 2013, pp. 1–4. DOI: 10.1109/PEDG.2013.6785604.

[25] Y. Zhang, N. Alatawneh, M.-C. Cheng, and P. Pillay, “Magnetic core losses measurement instrumentations and a dynamic hysteresis loss model,” Oct. 2009. DOI: 10.1109/EPEC.2009.5420918.

[26] Ž. Hederić, M. Barukčić, T. Benšić, D. Barešić, and A. Jahić, “Round rotational single sheet tester for rotational core loss measurements,” in *2017 International Conference on Smart Systems and Technologies (SST)*, 2017, pp. 321–326. DOI: 10.1109/SST.2017.8188718.

[27] *No25-1350h data sheet*, Tata Steel, Mar. 2019.

[28] L. Mthombeni and P. Pillay, “Core losses in motor laminations exposed to high-frequency or nonsinusoidal excitation,” *IEEE Transactions on Industry Applications*, vol. 40, no. 5, pp. 1325–1332, 2004. DOI: 10.1109/TIA.2004.834099.

A

Models

A.1 Permeability model

Table A.1: Initial coefficients for $\mu_r(B)$

Sample	α	β	γ	δ
B	$3.44e^{-06}$	$-52.15e^{-04}$	$23.60e^{-03}$	2965.69
C	$5.09e^{-07}$	$-11.33e^{-04}$	$-46.19e^{-02}$	2191.20
D	$-4.38e^{-07}$	$3.83e^{-04}$	$-57.48e^{-02}$	1645.70
E	$1.56e^{-07}$	$-15.77e^{-05}$	$-63.89e^{-02}$	1670.27
F	$-5.10e^{-07}$	$6.34e^{-05}$	$-18.29e^{-02}$	1126.70

Table A.2: Final coefficients for $\mu_r(B, x)$

Coefficients first fitting	**z = 1**	**z = 2**	**z = 3**
α_z	$-67.45e^{-03}$	$11.89e^{-04}$	$-2.25e^{-06}$
β_z	146.32	-2.21	$39.63e^{-04}$
γ_z	-79854.57	783.64	-1.75
δ_z	$14.08e^{+05}$	$27.13e^{+04}$	971.09

A.2 Iron loss model

Table A.3: Initial coefficients for $k_h(B)$

Sample	**u**	**v**	**w**
B	0.0220	-0.0603	0.0635
C	0.0194	-0.0686	0.0828
D	0.0249	-0.0860	0.0976
E	0.0383	-0.1155	0.1137
F	0.0401	-0.1226	0.1177

Table A.4: Initial coefficients for $k_e(B)$

Sample	**p**	**q**	**r**
B	$0.32e^{-04}$	$-0.68e^{-04}$	$0.58e^{-04}$
C	$0.51e^{-04}$	$-0.99e^{-04}$	$0.62e^{-04}$
D	$0.08e^{-03}$	$-0.15e^{-03}$	$0.08e^{-03}$
E	$0.44e^{-04}$	$-0.82e^{-04}$	$0.48e^{-04}$
F	$0.38e^{-04}$	$-0.67e^{-04}$	$0.38e^{-04}$

Table A.5: Final coefficients for $k_h(B, x)$

Coefficients first fitting	**z = 1**	**z = 2**	**z = 3**	**z = 4**
u_z	$-6.79e^{+04}$	$3.25e^{+03}$	-27.81	0.08
v_z	$1.42e^{+05}$	$-6.93e^{+03}$	63.99	-0.21
w_z	$-6.17e^{+04}$	$3.12e^{+03}$	-32.23	0.16

Table A.6: Final coefficients for $k_e(B, x)$

Coefficients first fitting	**z = 1**	**z = 2**	**z = 3**	**z = 4**
p_z	252.75	-11.73	0.0878	$-7.28e^{-05}$
q_z	-492.43	22.91	-0.17	$1.52e^{-04}$
r_z	206.60	-9.71	0.08	$-5.81e^{-05}$

A.3 Measurements

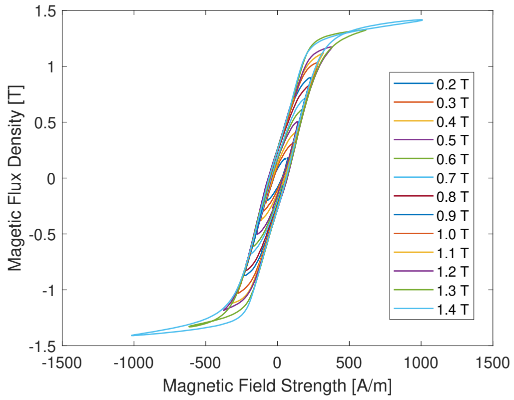

(a)

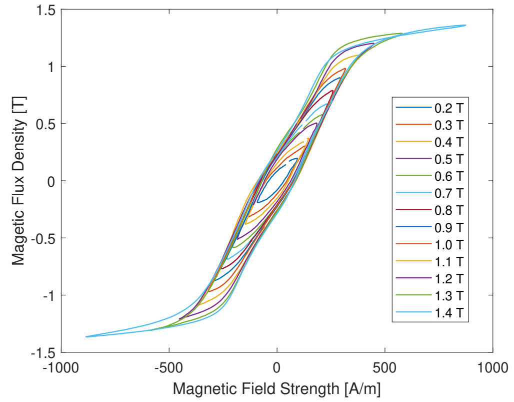

(b)

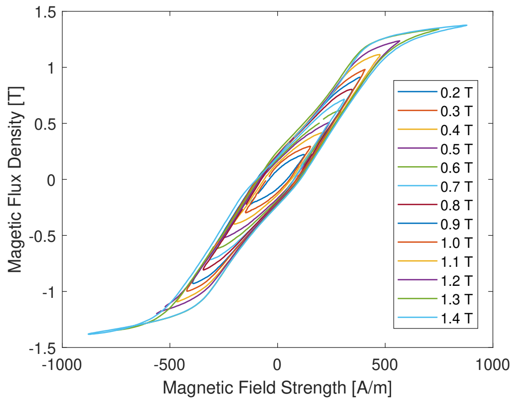

(c)

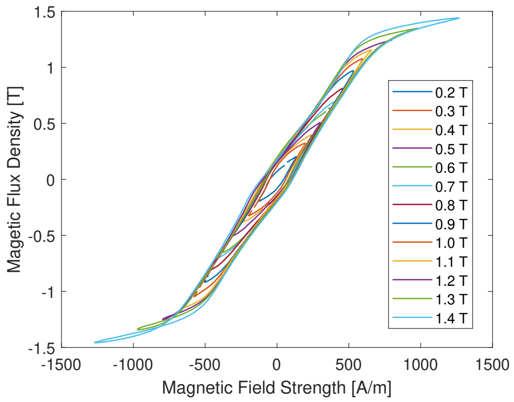

(d)

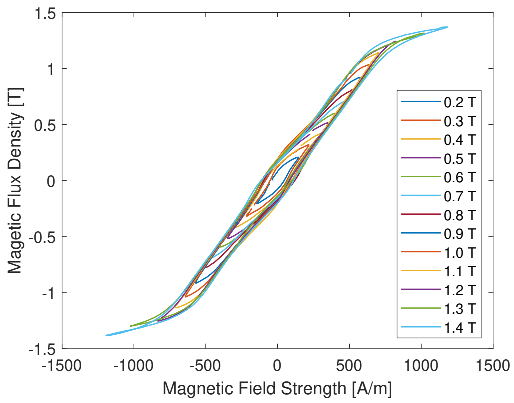

(e)

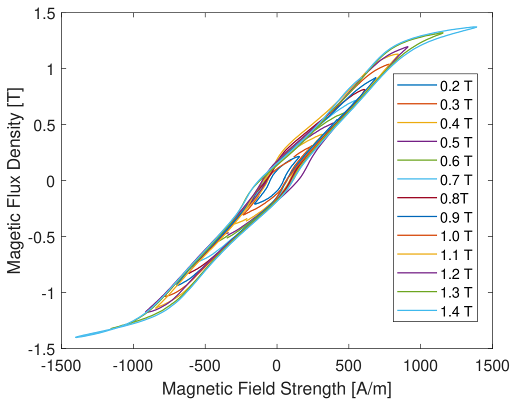

(f)

Figure A.1: Hysteresis loops at 200 Hz for (a) Sample A, (b) Sample B, (c) Sample C, (d) Sample D, (e) Sample E, (f) Sample F.

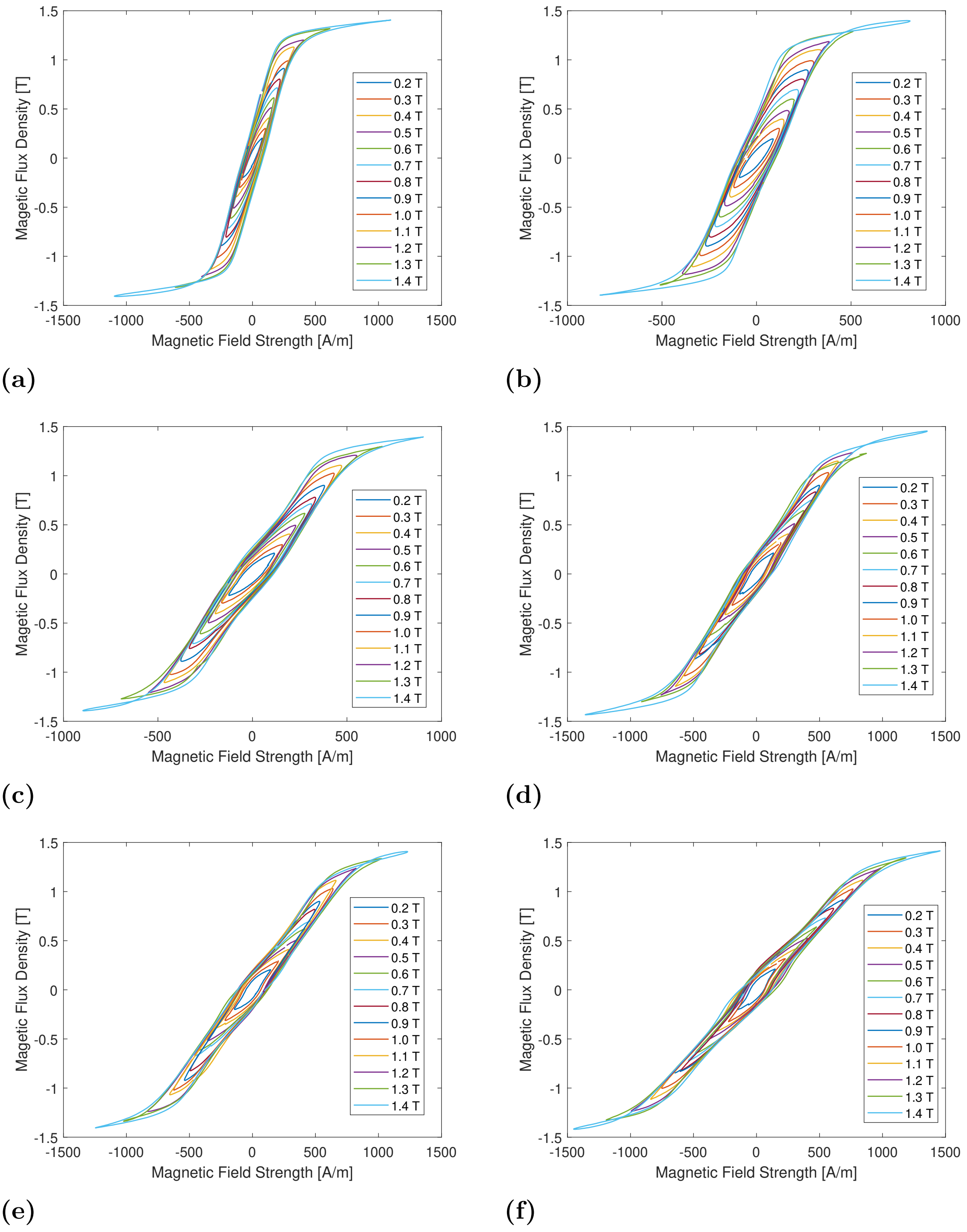

Figure A.2: Hysteresis loops at 300 Hz for (a) Sample A, (b) Sample B, (c) Sample C, (d) Sample D, (e) Sample E, (f) Sample F.

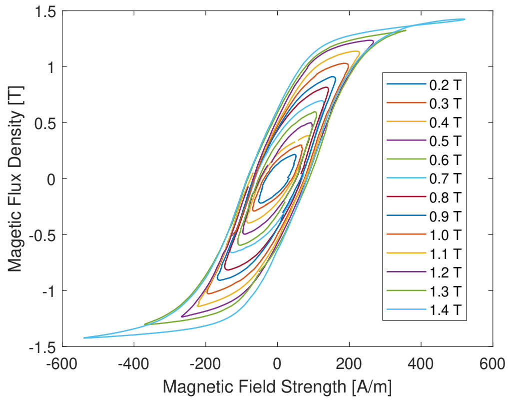

(a)

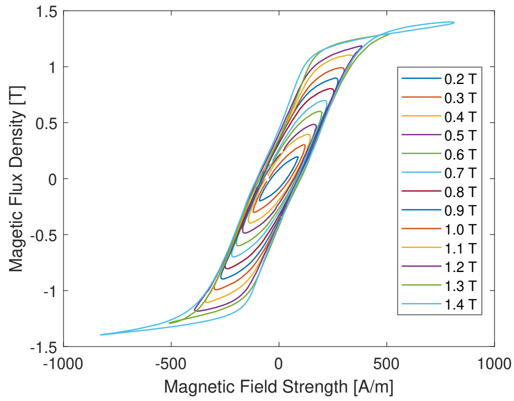

(b)

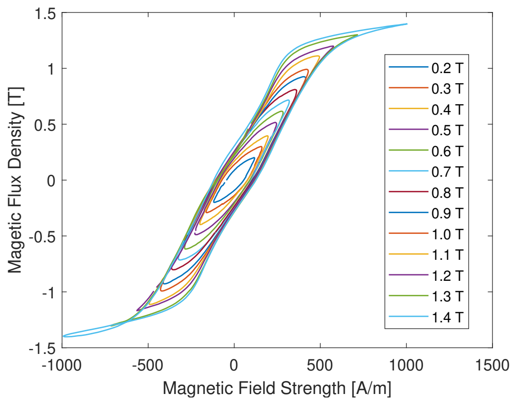

(c)

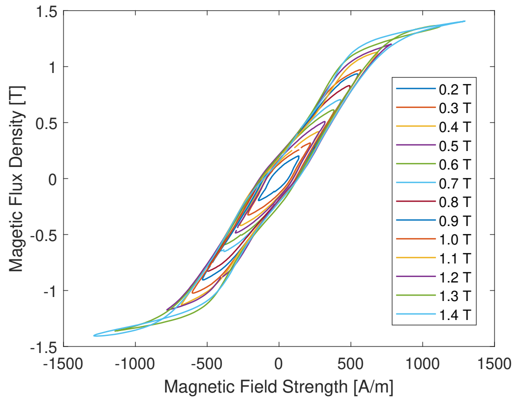

(d)

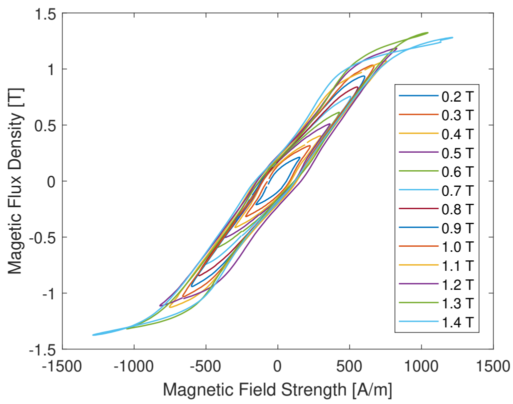

(e)

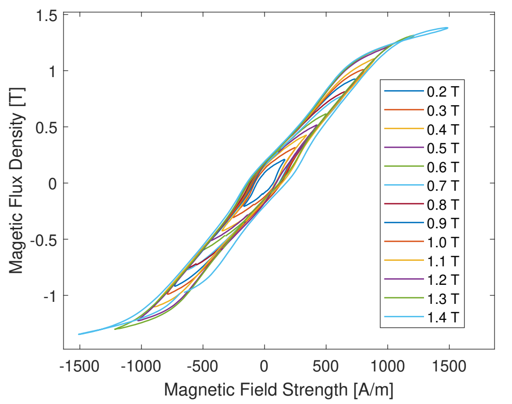

(f)

Figure A.3: Hysteresis loops at 400 Hz for (a) Sample A, (b) Sample B, (c) Sample C, (d) Sample D, (e) Sample E, (f) Sample F.

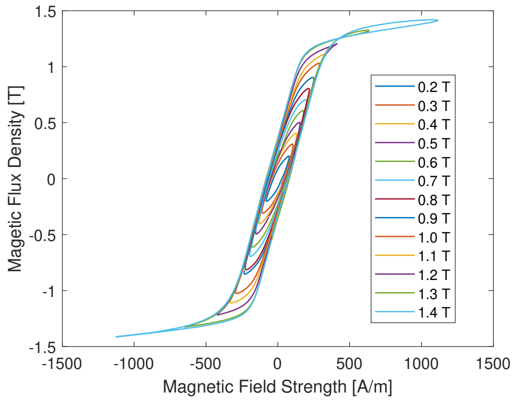

(a)

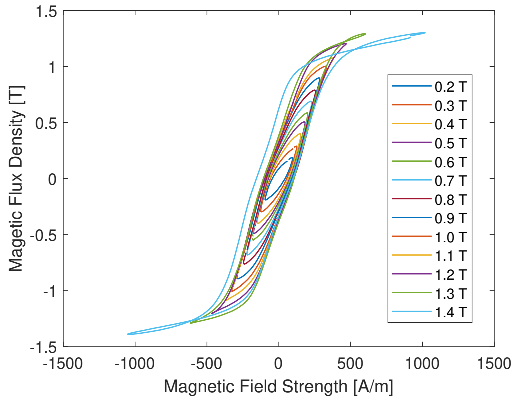

(b)

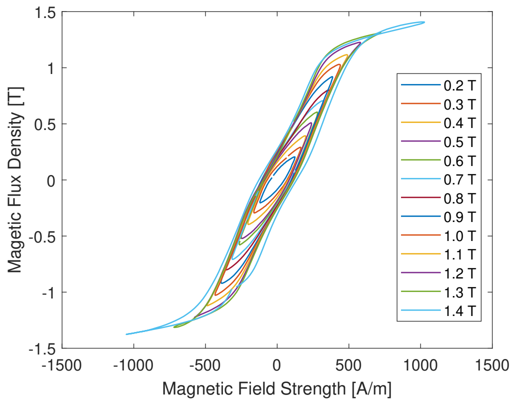

(c)

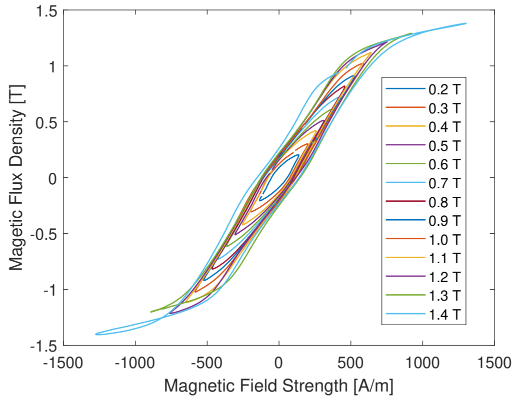

(d)

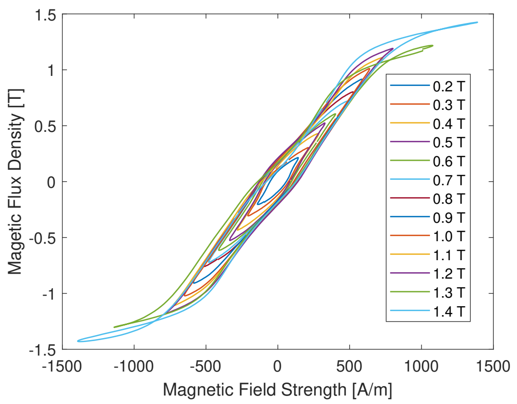

(e)

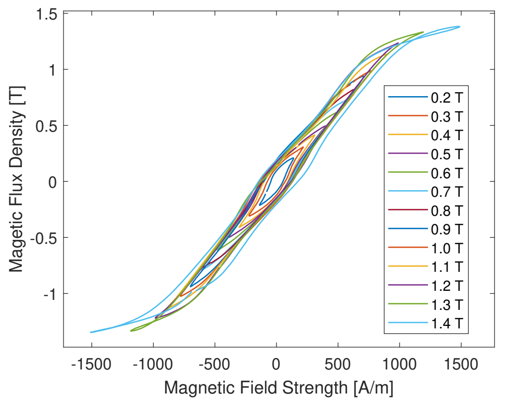

(f)

Figure A.4: Hysteresis loops at 500 Hz for (a) Sample A, (b) Sample B, (c) Sample C, (d) Sample D, (e) Sample E, (f) Sample F.

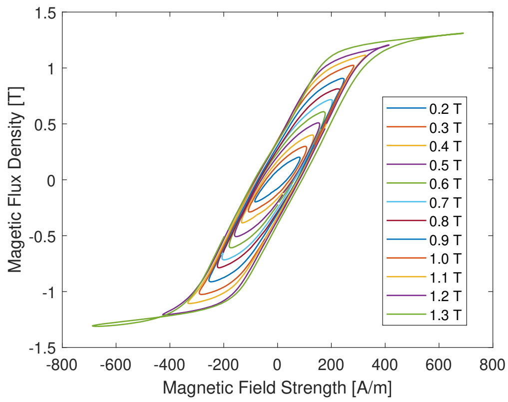

(a)

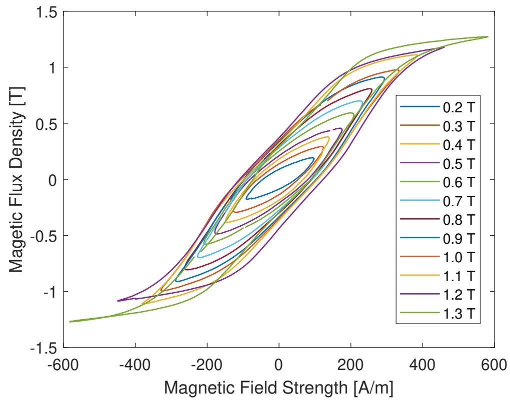

(b)

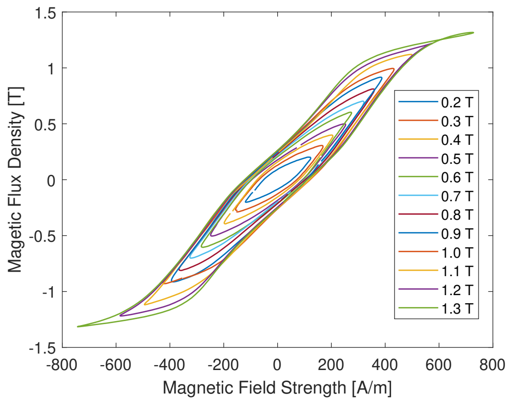

(c)

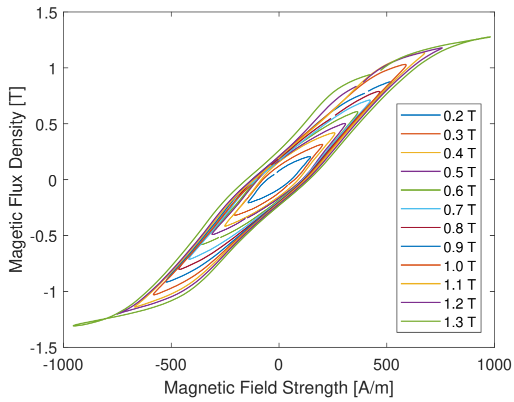

(d)

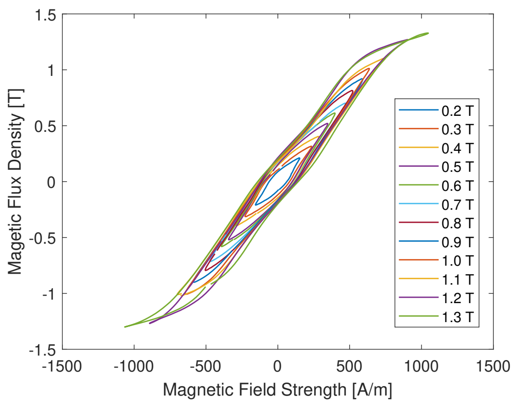

(e)

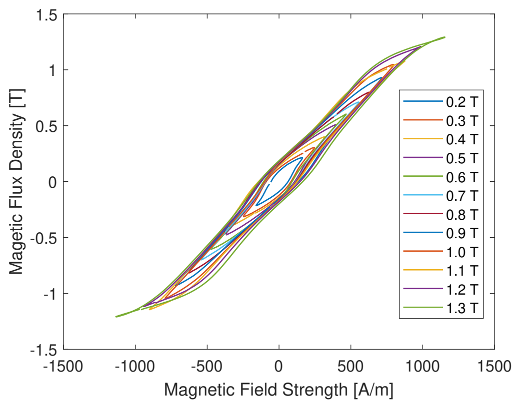

(f)

Figure A.5: Hysteresis loops at 600 Hz for (a) Sample A, (b) Sample B, (c) Sample C, (d) Sample D, (e) Sample E, (f) Sample F.

DEPARTMENT OF SOME SUBJECT OR TECHNOLOGY
CHALMERS UNIVERSITY OF TECHNOLOGY
Gothenburg, Sweden
www.chalmers.se

CHALMERS
UNIVERSITY OF TECHNOLOGY